The Astrophysical Journal, 833:231 (17pp), 2016 December 20 doi:10.3847/1538-4357/833/2/231

A SYSTEMATIC STUDY OF MID-INFRARED EMISSION FROM CORE-COLLAPSE SUPERNOVAE WITH SPIRITS

Samaporn Tinyanont[1], Mansi M. Kasliwal[1], Ori D. Fox[2], Ryan Lau[1,3], Nathan Smith[4], Robert Williams[2], Jacob Jencson[1], Daniel Perley[5], Devin Dykhoff[6], Robert Gehrz[6], Joel Johansson[7], Schuyler D. Van Dyk[8], Frank Masci[8], Ann Marie Cody[9], and Thomas Prince[1]
[1] Division of Physics, Mathematics and Astronomy, California Institute of Technology, Pasadena, CA 91125, USA; st@astro.caltech.edu
[2] Space Telescope Science Institute, 3700 San Martin Drive, Baltimore, MD 21218, USA
[3] Jet Propulsion Laboratory, California Institute of Technology, 4800 Oak Grove Drive, Pasadena, CA 91109, USA
[4] Steward Observatory, University of Arizona, Tucson, AZ 85721, USA
[5] Dark Cosmology Centre, Niels Bohr Institute, University of Copenhagen, Juliane Maries Vej 30, DK-2100 København Ø, Denmark
[6] Minnesota Institute for Astrophysics, School of Physics and Astronomy, University of Minnesota, 116 Church Street, S. E., Minneapolis, MN 55455, USA
[7] Benoziyo Center for Astrophysics, Weizmann Institute of Science, 76100 Rehovot, Israel
[8] Infrared Processing and Analysis Center, California Institute of Technology, M/S 100-22, Pasadena, CA 91125, USA
[9] NASA Ames Research Center, Moffett Field, CA 94035, USA
Received 2016 January 12; revised 2016 November 1; accepted 2016 November 5; published 2016 December 20

ABSTRACT

We present a systematic study of mid-infrared emission from 141 nearby supernovae (SNe) observed with *Spitzer*/IRAC as part of the ongoing SPIRITS survey. We detect 8 Type Ia and 36 core-collapse SNe. All Type Ia/Ibc SNe become undetectable within three years of explosion, whereas $22 \pm 11\%$ of Type II SNe continue to be detected. Five Type II SNe are detected even two decades after discovery (SN 1974E, 1979C, 1980K, 1986J, and 1993J). Warm dust luminosity, temperature, and a lower limit on mass are obtained by fitting the two IRAC bands, assuming an optically thin dust shell. We derive warm dust masses between 10^{-6} and $10^{-2}\,M_{\odot}$ and dust color temperatures between 200 and 1280 K. This observed warm dust could be pre-existing or newly created, but in either case represents a lower limit to the dust mass because cooler dust may be present. We present three case studies of extreme SNe. SN 2011ja (II-P) was over-luminous ($[4.5] = -15.6$ mag) at 900 days post explosion with increasing hot dust mass, suggesting either an episode of dust formation or intensifying circumstellar material (CSM) interactions heating up pre-existing dust. SN 2014bi (II-P) showed a factor of 10 decrease in dust mass over one month, suggesting either dust destruction or reduced dust heating. The IR luminosity of SN 2014C (Ib) stayed constant over 800 days, possibly due to strong CSM interaction with an H-rich shell, which is rare among stripped-envelope SNe. The observations suggest that this CSM shell originated from an LBV-like eruption roughly 100 years pre-explosion. The observed diversity demonstrates the power of mid-IR observations of a large sample of SNe.

Key words: supernovae: general – supernovae: individual (SN 2011ja, SN 2014C, SN 2014bi)

1. INTRODUCTION

The mid-infrared (mid-IR) evolution of core-collapse supernovae (CCSNe) has been studied in some events, but studies of a large sample containing multiple different SN subtypes have only become possible recently with multi-year observations by the *Spitzer Space Telescope*. A comprehensive and systematic study of a large sample of CCSNe across all types is essential to delineate the temporal evolution of a massive star after its explosive death. Mid-IR studies complement and expand on the body of knowledge obtained from extensive studies in optical and near-IR (see, e.g., Gerardy 2002; Bianco et al. 2014; Wheeler et al. 2015). One of the advantages of the mid-IR is that it is virtually free of dust extinction. Jencson et al. (2016) recently demonstrated that *Spitzer* can detect an SN entirely missed by optical surveys due to heavy host galaxy extinction. The mid-IR also traces emission from warm dust in the ejecta of a CCSN or in the circumstellar material (CSM) that is related to the progenitor star. CCSNe have long been proposed as major possible sources of dust production, especially in high-redshift galaxies where other possible dust factories (e.g., stellar winds of AGB stars) could not be in operation either because those galaxies were too young to form AGB stars or the stellar metallicity in that epoch was inadequate to form dust particles (Gall et al. 2011; Cherchneff 2014 and references therein). Theoretical models predict the mass of dust produced in CCSNe to be around $0.1–1\,M_{\odot}$, which is adequate for CCSNe to contribute significantly to the observed dust content in the early universe (Nozawa et al. 2003, 2008). Dust characteristics of SNe, such as grain size, mass, and temperature, can be quantified by analyzing the spectral energy distribution (SED) and the light curve of an SN (see, for example, Fox et al. 2010, 2011, 2013; Szalai & Vinkó 2013). Gehrz & Ney (1990) described three distinct signatures of dust formation that were observed in SN 1987A and that are expected to be generally observable in other SNe that form dust. (1) Optical spectral lines are asymmetrically blueshifted because the newly formed dust absorbs light coming from the receding side of the ejecta. (2) The decline rate of the optical light curves increases because the new dust causes more extinction in the *UBV* wavebands. (3) The emission in the mid-IR brightens due to thermal emission from warm dust, making it a more dominant component than the optical and near-IR.

A number of SNe have been identified as dust producers through observations in the mid-IR. For example, Helou et al. (2013) and Ergon et al. (2015) conducted mid-IR studies of the Type IIb SN 2011dh in Messier 51 (see Filippenko 1997 for more information on supernova classification). The time evolution of its SED showed that the mid-IR emission became

relatively brighter than optical emission at late times. The light curve also showed excess mid-IR emission that could not be explained by an IR echo alone, indicating an additional dust heating mechanism or the formation of new dust. Meikle et al. (2011) and Szalai et al. (2011) analyzed the Type II-P SN 2004dj and found a significant re-brightening ∼400 days post explosion. Similarly, Fabbri et al. (2011) studied the Type II-P SN 2004et and observed re-brightening at 1000 days after the explosion. In both cases, they inferred new dust formation by observing red-wing attenuation in optical spectral lines and the sharp rate of decline in the optical light curves. A mid-IR population study of 12 SNe II-P by Szalai & Vinkó (2013) found warm dust emission with an inferred dust mass of $\sim 10^{-3}\,M_{\odot}$. Fox et al. (2011, 2013) conducted a survey on all known 68 Type IIn events. These are CCSNe with narrow emission lines that are indicators of circumstellar interactions that either produce new dust or heat up pre-existing dust. They detected late time emission from 10 targets with an inferred dust mass of up to $10^{-2}\,M_{\odot}$. They concluded that most of the warm emitting dust was pre-existing. In addition to Type IIn SNe whose CSM interactions were discovered early on, recent late time observations reveal that many SNe interact with the CSM later in their evolution, providing additional channels for dust production. Andrews et al. (2016) presented spectroscopic evidence for CSM interactions in the Type II-P SN 2011ja at 64–84 days post explosion accompanied by an episode of dust production between the forward and the reverse shocks. These interactions with dust production have also been observed in a small number of Type Ibc SNe, such as SN 2006jc (see, e.g., Foley et al. 2007; Mattila et al. 2008; Smith et al. 2008; Sakon et al. 2009 and references therein).

The mass of newly formed dust observed in a number of CCSNe is significantly lower than dust masses predicted by theoretical models, falling between 10^{-3} and $10^{-4}\,M_{\odot}$ per event instead of 0.1 and $1\,M_{\odot}$ (see, in addition, Andrews et al. 2010; Gall et al. 2014). It has been shown, however, that the large amount of dust associated with CCSNe is too cold to be detected in the mid-IR. Recent studies of SN 1987A and other supernova remnants (SNRs) reveal a large amount of dust emitting in the far-IR and submillimeter wavelengths. Matsuura et al. (2015) used the *Herschel Space Observatory* (Pilbratt 2003) to observe SN 1987A and deduced, depending on dust composition, $0.5–0.8\,M_{\odot}$ of cold dust in the remnant. Indebetouw et al. (2014) used the Atacama Large Millimeter/Submillimeter Array (Brown et al. 2004) to observe SN 1987A at high spatial resolution and confirmed that $>0.2\,M_{\odot}$ of dust was formed in the inner ejecta and was neither heated by CSM interactions as suggested by some authors (e.g., Bouchet & Danziger 2014), nor pre-existing. This dust mass is consistent, but is orders of magnitude higher than the $\sim 10^{-4}\,M_{\odot}$ lower limit derived by Wooden et al. (1993) two years post explosion. This suggests that bulk of the dust condensed late in the evolution of this particular SN. Alternatively, Dwek & Arendt (2015) suggested that the dust was hidden in the optically thick part of the ejecta at early times (<1000 days), and hence, not observed until later. The presence of about $0.1\,M_{\odot}$ of cold dust was also suggested by far-infrared and submillimeter observations of nearby SNRs, Cassiopeia A (Barlow et al. 2010) and the Crab Nebula (Gomez et al. 2012). Recently, Lau et al. (2015) reported that $0.02\,M_{\odot}$ of ejecta-formed dust has survived in the 10,000 year old SNR Sgr A East. These results demonstrate that a large fraction of the dust formed in the inner core of an SN can survive the reverse shocks and later be dispersed into the interstellar medium.A large fraction of the newly formed dust appears to emit at longer wavelengths, however, observations in two IRAC bands of warm *Spitzer* are sensitive to only a small, relatively hot fraction of that dust. Nevertheless, these observations are still powerful tools for identifying SNe with dust formation or CSM interactions, which heat pre-existing dust to high temperatures.

This work seeks to study a comprehensive sample of different types of CCSNe observed with *Spitzer* at a variety of epochs after explosion in order to construct an overview of the mid-IR time evolution of these events. This work complements the mid-IR light-curve templates that have already been compiled for Type Ia SNe (Johansson et al. 2014). The collage of light curves from a number of well-observed Type Ia SNe shows that these events are homogeneous in their time evolution. In this paper, we compile a light-curve collage for CCSNe in order to identify the typical time evolution of these events and to potentially uncover some unusual SNe. A simple one-component, graphite dust model is fitted to the SED to extract the luminosity, temperature, and mass of warm dust emitting in the mid-IR. We emphasize here that our observations are only sensitive to warm dust with a temperature of more than a few hundred Kelvin. Many SNe are observed at several epochs, allowing us to trace the time evolution of dust parameters. In Section 2, we discuss the SPIRIT survey in more detail along with the SN sample in galaxies covered by SPIRITS. We present the demographics of the SNe and light-curve collages for Type Ib/c and II SNe and identify and discuss events that are outliers in Section 3. We extract and present dust parameters for each observation in this section. In Section 4, we present four intriguing case studies: the over-luminous Type II SN 2011ja, the re-brightening Type Ib SN 2014C, the under-luminous and extremely red Type II-P SN 2014bi, and a sample of senior SNe with mid-IR emission detected more than 20 years after their explosions.

2. OBSERVATIONS

2.1. The Supernova Sample and Spitzer/IRAC Photometry

The SPitzer InfraRed Intensive Transients Survey (SPIRITS; M. M. Kasliwal et al. 2016, in preparation) targets 190 nearby galaxies within 20 Mpc to a depth of 20 mag. The observations are performed in the 3.6 μm and 4.5 μm bands of the InfraRed Array Camera (IRAC, Fazio et al. 2004) on board the warm *Spitzer Space Telescope* (Werner et al. 2004; Gehrz et al. 2007). Magnitudes in both bands are denoted as [3.6] and [4.5] hereafter. All magnitudes are in the Vega system and the conversion $m_{\rm AB} - m_{\rm Vega}$ is +2.78 for [3.6] and +3.26 for [4.5] computed from the zero points given in the IRAC Instrument Handbook. The SPIRITS galaxy sample has hosted 141 SNe in total since the year 1901, and these SNe have been observed with *Spitzer* in at least one epoch.[10] With the combination of archival data and new SPIRITS observations, 44 SNe are detected: 8 are Type Ia, 9 are Type Ib/c, and the remaining 27 are Type II. Seven new SNe exploded in this galaxy sample during 2014. All of them are observed and 6 are detected. The non-detection, SN 2014bc, is inside its host's nucleus and all observations of it are saturated. Two Type Ia

[10] The SN list is obtained from the IAU Central Bureau for Astronomical Telegram at http://www.cbat.eps.harvard.edu/lists/Supernovae.html.

events, SN 2014J and SN 2014dt, are discussed in detail in Johansson et al. (2014) and Fox et al. (2016), respectively.

We used a combination of data from new SPIRITS observations and from other programs, both publicly available from the *Spitzer* Heritage Archive, to study mid-IR emission from the SNe of Type Ib/c and different subtypes of Type II. We used Post Basic Calibrated Data (pbcd), which had been coadded and calibrated by the standard pipeline. The SPIRITS pipeline performs PSF matching image subtraction using stacks of archival *Spitzer* data, generally ranging from 2004–2008, as references. The actual range of epochs used as reference depends on the availability of the data for each host galaxy.

For 34 out of 44 SNe that exploded after this range of epochs, there is no SN light present in the reference frames. In this case, the aperture photometry is performed on the subtracted image to eliminate the flux contribution from the galaxy background, which is bright and spatially varying. This methodology is applied to every epoch of each SN for which a pre-explosion reference image exists. We checked our photometry against IRAC photometry of SN 2011dh presented by Ergon et al. (2015) between 18 and 1061 days post explosion. The results agree to within 5%. Twelve SNe of Type Ib/c and II that are detected and have reliable photometry (i.e., not too close to the host's nucleus) are shown in boldface in Table 1 and are used further in our analysis in Sections 3.2 and 3.3. In some epochs of SN 2011ja, the SN location is near the edge of the frame and the pipeline fails to produce good subtraction images. We instead use aperture photometry on all frames, then subtract the average baseline flux in pre-explosion images from each epoch in which the SN appears. This method provides good agreement with the image subtraction method in other epochs where we have high-quality subtractions.

For SNe whose reference frames were contaminated with SN light, we searched for a distinct point source at the location of an SN directly in the science frame to judge whether or not we had a detection. In cases judged to be detections, forced aperture photometry with sky background subtraction was performed on the science frames. The aperture corrections from the IRAC Instrument Handbook were then applied. Because the galaxy background could not be completely eliminated in these cases, the photometric data had larger uncertainties, especially at late times when the SN light was comparable in brightness to the background. In order to ascertain the detection, the thumbnails of every observation of every SN were visually vetted. We excluded SN impostors SN 1997bs and SN 2008S (Kochanek et al. 2012; Adams & Kochanek 2015). We also excluded SNe that were located near their host's nucleus, as all observations were saturated (e.g., SN 2004am, 2008iz, and 2014bc). By doing image subtraction, we were able to identify mid-IR light from old and slowly evolving SNe that had escaped notice in previous works because they were very dim in comparison to the background (see, e.g., Table 1 in Fox et al. 2011). All SNe with at least one detection by *Spitzer*, either with the new data from SPIRITS or from other programs, are presented in Table 1.

2.2. Near-infrared Photometry

As part of the follow-up campaign accompanying SPIRITS, some of the recent SNe listed in Table 1 were observed in near-IR from multiple observatories. SN 2013bu, SN 2013df, SN 2014C, and SN 2014bi were observed in the J, H, and Ks bands using the Two Micron All-Sky Survey spectrometer (2MASS; Milligan et al. 1996) on the 60 inch telescope at the University of Minnesota's Mount Lemmon Observing Facility (MLOF; Low et al. 2007). The science frame and the surrounding sky are observed alternately for sky subtraction. No SNe were detected, so the limiting magnitudes (5σ) are given in Table 2. SN 2014C was observed in the J, H, and Ks bands using the $4' \times 4'$ Nordic Optical Telescope Near-Infrared Camera and Spectrograph (NOTCam; Abbott et al. 2000) at the Nordic Optical Telescope under the programme 51-032 (PI: Johansson). We used the wide-field imaging mode and beam-switching to guarantee successful sky subtraction. Data reduction was performed with the NOTCam Quick-Look reduction package based on IRAF. PSF fitting photometry was performed on the sky-subtracted frames, which were then calibrated using 2MASS stars in the field. SN 2014C was also observed in the Ks band using the Wide-Field InfraRed Camera (WIRC; Wilson et al. 2003) on the 200 inch Hale Telescope at Palomar Observatory. The data were sky subtracted and calibrated using 2MASS stars in the field. The resulting photometry is listed in Table 2.

3. RESULTS

3.1. Demographics

The detection statistics for each type of SNe are presented in Figure 1. We consider separately three time bins after discovery: less than one year, one to three years, and more than three years. In each bin, if an SN is observed with at least one detection, it is marked as detected, even though it might fade to non-detection later in the same bin. Otherwise, if all observations of an SN in that bin result in non-detections, then that SN is marked as a non-detection. The number of detections and non-detections of each type of SN in each bin is then tallied up. The error estimates for small-number statistics are done using the method described in Cameron (2011) based on Bayesian statistics.

The distance to an SN affects our sensitivity to detect the event. When one considers a given type of SN, events further away tend to fall off the detection limit first. However, across different types, the distance distributions in our sample are similar. As a result, the different detection statistics we find for each type of SN are not only on account of the Malmquist bias (the preferential detection of intrinsically bright objects). In other words, the relative fraction of detected Type II SNe versus Type Ia SNe at late time is not due to the distance distribution. The results reflect the intrinsic difference in mid-IR evolution between CCSNe and Type Ia SNe.

The results show that almost all SNe across all types are detected within one year after discovery. The only two exceptions are Type Ia SN 2004W and SN 2011B. Both SNe were undetected in both IRAC channels six and ten months, respectively, after their discovery dates. Overall, the mid-IR emission from most Type Ia SNe in our sample is shorter lived compared to CCSNe. We note that our sample does not include Type Ia events with CSM interactions (Ia-CSM), in which case mid-IR emission lasts longer (see, e.g., SN 2005gj and SN 2002ic, Fox & Filippenko 2013; SN 2014dt Fox et al. 2016).

Between one and three years after discovery, the fractions of Type Ia and Ib/c detected dropped dramatically, to $22 \pm 24\%$ and $55 \pm 28\%$, respectively. However, most Type II SNe ($82 \pm 18\%$) continued to be detected. As discussed above, this

Table 1
SN Sample

Name	Type	Discovery	R.A. (J2000)	Decl. (J2000)	Host	d (Mpc)	Reference
1974E	II	1974 Mar 21	180.475	−18.866667	NGC 4038	20.04	…
1979C	II-L	1979 Apr 19	185.744292	15.797694	NGC 4321	17.95	Dwek (1983)
1980K	II-L	1980 Oct 28	308.875292	60.106611	NGC 6946	6.67	Dwek (1983), Dwek et al. (1983)
1986J	II	1986 Aug 21	35.630417	42.3325	NGC 891	8.36	Cappellaro & Turatto (1986), Milisavljevic et al. (2008)
1993J	IIb	1993 Mar 28	148.854167	69.020278	NGC 3031	3.63	Filippenko et al. (1993)
1999bw	IIn	1999 Apr 20	154.945042	45.526389	NGC 3198	11.64	Sugerman et al. (2004)
2003gd	II-P	2003 Jun 12	24.177708	15.739139	NGC 628	8.59	Sugerman et al. (2006), Meikle et al. (2007)
2003hn	II-P	2003 Aug 25	56.150417	−44.630278	NGC 1448	13.43	Salvo et al. (2003), Szalai & Vinkó (2013)
2003J	II-P	2003 Jan 11	182.7405	50.4755	NGC 4157	14.32	Ayani et al. (2003), Szalai & Vinkó (2013)
2004cc	Ic	2004 Jun 10	189.143333	11.242444	NGC 4568	33.73	Foley et al. (2004)
2004dj	II-P	2004 Jul 31	114.320917	65.599389	NGC 2403	3.18	Meikle et al. (2011), Szalai et al. (2011)
2004et	II	2004 Sep 27	308.855542	60.121583	NGC 6946	6.67	Kotak et al. (2009), Fabbri et al. (2011)
2004gn	Ib/c	2004 Dec 01	188.550417	2.659556	NGC 4527	9.68	Pugh & Li (2004)
2005ae	IIb?	2005 Feb 01	119.566	−49.855528	ESO 209-9	12.30	Filippenko & Foley (2005)
2005af	II-P	2005 Feb 08	196.183583	−49.566611	NGC 4945	3.80	Kotak et al. (2006), Szalai & Vinkó (2013)
2005at	Ic	2005 Mar 15	287.473208	−63.823	NGC 6744	7.69	Kankare et al. (2014)
2005cs	II-P	2005 Jun 28	202.469917	47.176583	NGC 5194	7.66	Szalai & Vinkó (2013)
2005df	Ia	2005 Aug 04	64.407708	−62.769306	NGC 1559	10.76	Salvo et al. (2005), Diamond et al. (2015)
2006mq	Ia	2006 Oct 22	121.551625	−27.562611	ESO 494-G26	11.12	Duszanowicz et al. (2006)
2006ov	II-P	2006 Nov 24	185.480417	4.487972	NGC 4303	18.45	Szalai & Vinkó (2013)
2006X	Ia	2006 Feb 04	185.724958	15.809194	NGC 4321	17.95	Lauroesch et al. (2006), Wang et al. (2008)
2007it	II	2007 Sep 13	214.606792	−43.381611	NGC 5530	12.94	Andrews et al. (2011)
2007 sr	Ia	2007 Dec 18	180.47	−18.972694	NGC 4038	20.04	Pojmanski et al. (2008)
2009hd	II-L	2009 Jul 02	170.070667	12.979611	NGC 3627	10.81	Elias-Rosa et al. (2011)
2010br	Ib/c	2010 Apr 10	180.795625	44.528639	NGC 4051	22.39	Maxwell et al. (2010)
2011dh	IIb	2011 Jun 01	202.521333	47.169667	NGC 5194	7.66	Helou et al. (2013), Ergon et al. (2015)
2011fe	Ia	2011 Aug 24	210.774208	54.273722	Messier 101	7.38	McClelland et al. (2013)
2011ja	II-P	2011 Dec 10	196.296333	−49.524167	NGC 4945	3.80	Andrews et al. (2016)
2012aw	II-P	2012 Mar 16	160.974	11.671639	NGC 3351	8.79	Siviero et al. (2012)
2012cc	II	2012 Apr 29	186.736708	15.045972	NGC 4419	13.49	Marion et al. (2012b)
2012cg	Ia	2012 May 17	186.803458	9.420333	NGC 4424	7.31	Marion et al. (2012a)
2012fh	Ib/c	2012 Oct 18	160.891875	24.891389	NGC 3344	19.05	Nakano et al. (2012)
2013ai	II	2013 Mar 01	94.076458	−21.375806	NGC 2207	14.26	Conseil et al. (2013)
2013am	II	2013 Mar 21	169.737292	13.063722	NGC 3623	18.54	Nakano et al. (2013)
2013bu	II	2013 Apr 21	339.259042	34.401444	NGC 7331	13.12	Itagaki et al. (2013)
2013df	IIb	2013 Jun 07	186.622208	31.227306	NGC 4414	20.51	Morales-Garoffolo et al. (2014), Szalai et al. (2016)
2013dk	Ic	2013 Jun 22	180.469667	−18.87175	NGC 4038	20.04	Elias-Rosa et al. (2013)
2013ee	II	2013 Jul 13	150.486792	55.695556	NGC 3079	14.86	Cortini et al. (2013)
2013ej	II-P	2013 Jul 25	24.200667	15.758611	NGC 628	8.59	Bose et al. (2015)
2014bi	II-P	2014 May 31	181.512458	47.492639	NGC 4096	11.27	Kumar et al. (2014)
2014C	Ib	2014 Jan 05	339.273333	34.408861	NGC 7331	13.12	Kim et al. (2014), Milisavljevic et al. (2015)
2014df	Ib	2014 Jun 03	56.099958	−44.668917	NGC 1448	13.43	Monard et al. (2014)
2014dt	Ia-p	2014 Oct 29	185.489875	4.471806	NGC 4303	18.45	Fox et al. (2016)
2014J	Ia	2014 Jan 21	148.925583	69.673889	NGC 3034	3.52	Johansson et al. (2014)
2014L	Ic	2014 Jan 26	184.702833	14.412083	NGC 4254	16.83	Yamaoka et al. (2014)

Note. SNe in this sample are detected by *Spitzer* for at least one epoch. Bold are CCSNe with pre-explosion images for image subtraction.

is not a result of the distance bias in the sample. In fact, three out of four detected Type Ib/c events in this bin are further away than all four non-detected ones.

Finally, after three years, none of the Type Ia and Ib/c SNe were detected. However, 22 ± 11% of the Type II events remained detected, mostly in the 4.5 μm band. These long-lived events are SN 1974E (II), SN 1979C (II-L), SN 1986J (IIn), SN 1993J (IIb), SN 1999bw (IIn; Filippenko et al. 1999; Kochanek et al. 2012), SN 2004dj (II-P), SN 2004et (II-P), SN 2007it (II-P), SN 2009hd (II-L), and 2011ja (II-P; Andrews et al. 2016). Additional discussion of a well-sampled subset of these old SNe follows in Section 4.4. It is worth noting that the SN impostors, SN 1997bs and SN 2008S, were detected in our observations more than three years post-discovery, outlasting many other real Type II events, even though they are not particularly nearby. Because late-time mid-IR emission comes mostly from warm dust, this data set allows us to probe evolution of warm dust properties in these CCSNe.

3.2. Light Curves

3.2.1. Type Ib/c SNe

The light curves of all four Type Ib/c SNe for which we have image-subtracted photometry are shown in Figure 2. The data coverage spans epochs from 40 to 800 days after discovery, with multi-epoch data for SN 2013dk (Ic), SN 2014L (Ic), and SN 2014C (Ib). The projected peak brightness range from [4.5] = −18.3 and [3.6] = −18.3 mag

Table 2
Near-IR Photometry of the SNe

MJD	Epoch Days	*J*	*H*	*Ks*	Instrument
		SN 2013bu (II)			
56809	405.5	>16.1	>15.5	>15.1	MLOF/2MASS
56901	497.5	>16.2	>15.5	>15.3	MLOF/2MASS
56931	527.5	>16.1	>15.3	>14.9	MLOF/2MASS
56950	546.5	…	…	>19.0	P200/WIRC
56962	558.5	>16.1	>15.1	>14.5	MLOF/2MASS
		SN 2013df (IIb)			
56717	266.5	>15.9	>14.9	>14.9	MLOF/2MASS
57023	572.5	>14.5	>13.7	>13.9	MLOF/2MASS
		SN 2014C (Ib)			
56809	146.5	>13.4	>12.7	>12.1	MLOF/2MASS
56901	238.5	>13.9	>13.0	>12.6	MLOF/2MASS
56931	268.5	>13.5	>12.8	>12.3	MLOF/2MASS
56950	287.5	…	…	14.38(0.06)	P200/WIRC
56962	299.5	>13.5	>12.5	>12.3	MLOF/2MASS
57292	630.5	18.0 (0.1)	16.6 (0.1)	14.9 (0.1)	NOT/NOTCam
		SN 2014bi (II-P)			
57113	304.5	…	>14.8	>15.3	MLOF/2MASS

Note. This table summarizes all near-infrared photometry of the SNe in Table 1. Magnitudes listed are Vega, calibrated using 2MASS stars.

for SN 2014L to [4.5] = −19.7 and [3.6] = −19.0 for SN 2014C. The decline rate for SN 2014C is 0.5 mag/100 days in both channels within 200 days after the explosion. The two Type Ic events decay at roughly the same rates in [4.5]: about 0.8 mag/100 days within 450 days. However, the [3.6] decline rates for these events are quite different. SN 2014L decays for 1 mag/100 days out to 200 days, while SN 2013dk only decays at the rate of 0.68/100 days between 250 and 430 days. SN 2014df (Ib) is about 3.5 mag dimmer than SN 2014C, another Ib event, at the same epoch, but the lack of concurrent photometry yields no color information. No further observations of this galaxy have been made since 2015. The most interesting Type Ib/c SN observed in our sample is SN 2014C, which re-brightens by 0.15 mag in 4.5 μm and 0.24 mag in 3.6 μm around 250 days. It was observed again more than a year later at 620 days to be even brighter in both bands then maintained nearly constant luminosity out to 800 days. This peculiar time evolution in the mid-IR sets this event apart from other SNe in this sample. Further discussions of this SN are presented in Section 4.2. We also note that, apart from the peculiar Type Ib SN 2006jc with strong CSM interaction (see Mattila et al. 2008; Smith et al. 2008), dust emission has not been detected for any other Type Ib/c events.

3.2.2. Type II SNe

The light curves of all eight Type II SNe for which we have image-subtraction photometry are presented in Figure 3. SN 2011dh has the most well-sampled light curves covering epochs from pre-maximum to 1200 days after the detection, providing a template with which other SNe can be compared. Helou et al. (2013) interpolated [4.5] data to fill in the visibility gap between 90 and 250 days and found that SN 2011dh left its initial plateau into a decay at 150 ± 25 days post explosion. Between 200 and 400 days, SN 2011dh has steep decline rates of 1.96 and 1.57 mag/100 days at 3.6 μm and 4.5 μm, respectively. After 400 days, the light curves in both bands plateau to decline rates of 0.57 and 0.75 mag/100 days at 3.6 μm and 4.5 μm, respectively. After 600 days, the decline rates decrease to only 0.02 mag/100 days in both channels. In these epochs after 100 days, Helou et al. (2013) reported that an IR echo alone cannot account for the flux and that dust formation, additional heating mechanisms, a nearby interstellar cloud, or line or band emission must contribute. Ergon et al. (2015) reported the fractional increase of 3.6 μm, 4.5 μm, and K bands luminosity compared to optical in conjunction with an increase in the decline rate of the optical pseudo-bolometric light curve. They also observed small blueshifts in the [O I] and [Mg I] lines at 415 days. These results suggest that new dust is being created inside the expanding shell of ejecta attenuating optical light coming from the receding side of the shell.

The collage in Figure 3 shows heterogeneity in the Type II light curves in comparison with SN 2011dh. Some SNe—such as SN 2013bu (II), SN 2013df (IIb), and SN 2013ej (II-P)—have similar temporal evolution as that of SN 2011dh in terms of the absolute magnitudes, which are within 1 mag of SN 2011dh, and the decline rates. SN 2013ai shows similar plateauing after 400 days at 4.5 μm to a decline rate of 0.23 mag/100 days, but there is insufficient coverage in the 3.6 μm band. For a detailed discussion of SN 2013df, see Szalai et al. (2016).

SN 2013am and SN 2011ja (Andrews et al. 2016) re-brighten in different epochs. SN 2013am re-brightens slightly in the 4.5 μm band at around 370 days post-discovery, but not in the 3.6 μm band. SN 2011ja stays luminous from 100 to 400 days with higher fluxes at 400 days. It is possible for the SN to have rebrightened between 100 and 400 days. The secondary peak in the mid-IR has been observed in other Type II events, but at later times. Meikle et al. (2011) and Szalai et al. (2011) observed a re-brightening of SN 2004dj (II-P) in all

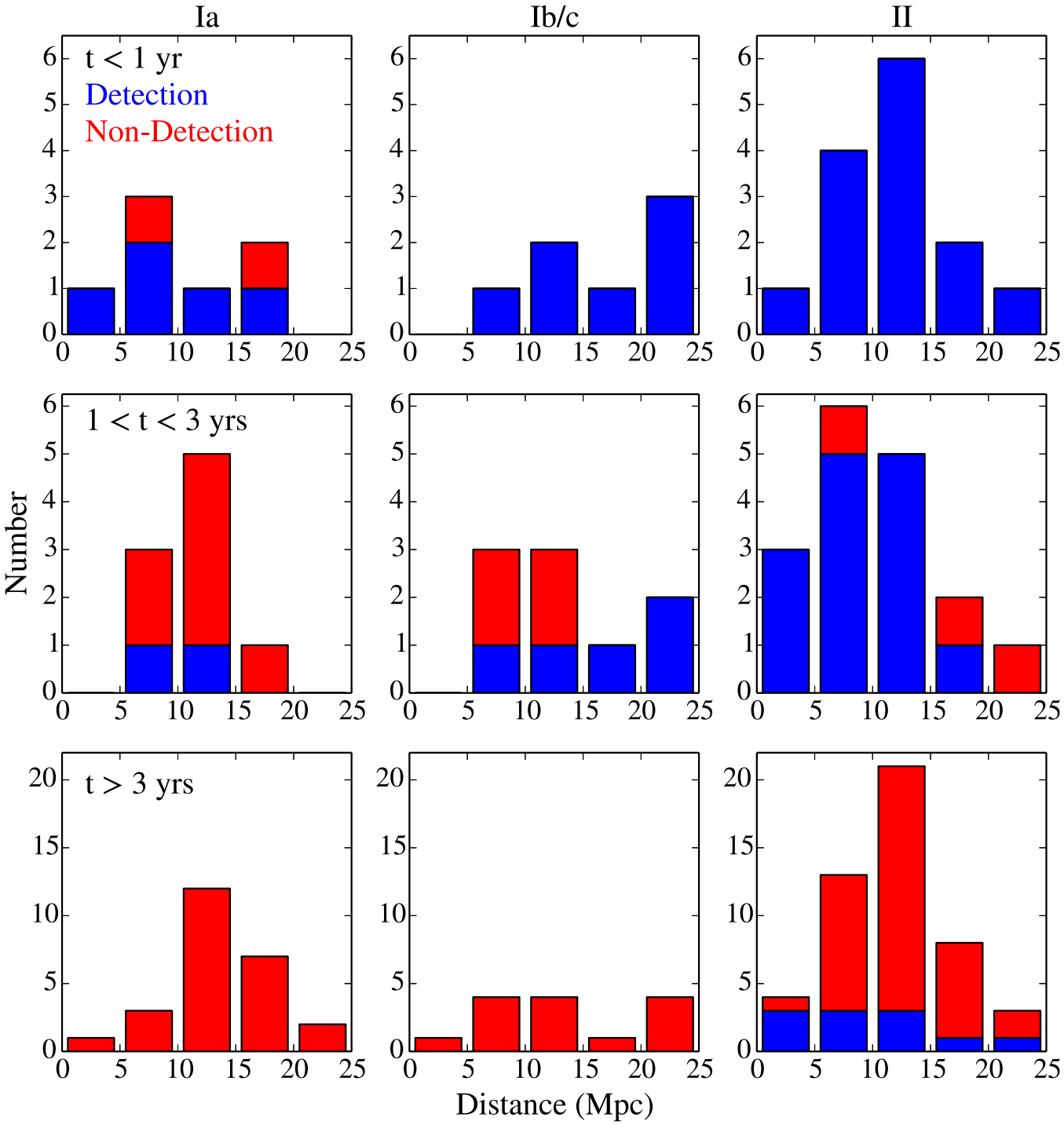

Figure 1. Stacked histograms showing detection statistics in our SN sample. Each column represents one type of SN and each row represents one bin of time after first discovery. Due to the small number of counts in our sample, we follow the procedure described by Cameron (2011) based on a Bayesian approach to estimating uncertainties.

IRAC bands, except the 4.5 μm, in the 16 μm and 22 μm bands of IRS Peak-Up Imaging (IRS-PUI) and 24 μm MIPS at 450–800 days post explosion with the shorter wavelengths peaking first. The absence of a secondary peak in the 4.5 μm band was attributed to a strong contribution from CO 1-0 vibrational band at 4.65 μm before 500 days. Fabbri et al. (2011) reported a secondary mid-IR peak for SN 2004et (II-P) in all IRAC bands, 16 μm IRS-PUI, and 24 μm MIPS at 1000 days. For both II-P events, attenuation in the red-wing of spectral lines and an increase in optical light curve decline rates were observed as the mid-IR light curves started to rise again. This strongly suggested that the re-brightening was due to dust production in the ejecta of these SNe. However, in the case of SN 2013am, where we do not have spectroscopic data, other sources of mid-IR flux, such as additional heating mechanisms and CSM interactions, cannot be ruled out. We also note that the amplitude of SN 2013am's re-brightening is very small compared to that observed in SN 2004dj and SN 2004et. The interesting case of SN 2011ja will be discussed in Section 4.1.

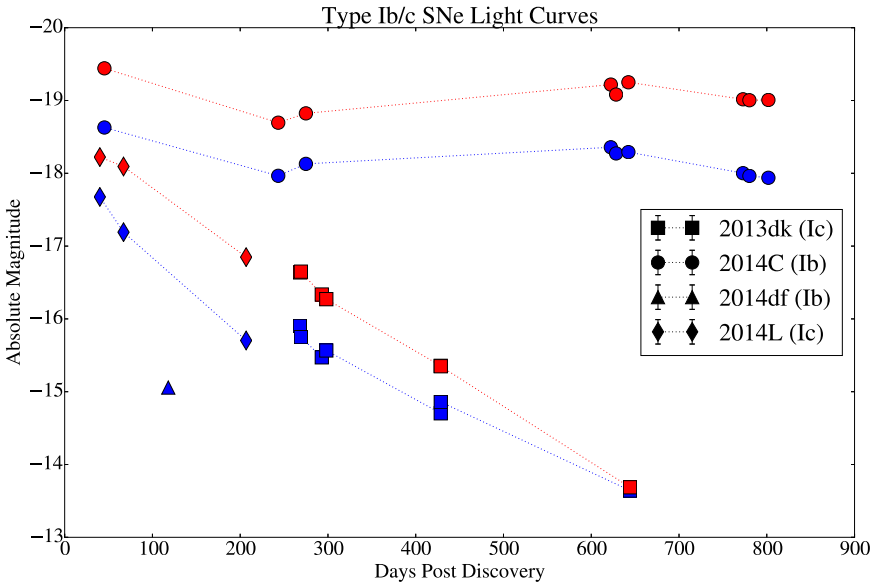

Figure 2. Collage of light curves of Type Ib/cI SNe with photometry based on image subtraction. Red and blue markers represent [4.5] and [3.6], respectively. The error bars are smaller than the plotting symbols.

In addition to the re-brightening events, another outlier is evident in the light curves collage shown in Figure 3. SN 2014bi (II-P) is under-luminous, especially in the 3.6 μm band in which it is 3–4 mag dimmer than other SNe. The color [3.6]–[4.5] is as much as 2.95 mag at 264 days. This event will also be discussed in detail in Section 4.3.

3.3. The SED and Dust Parameter Fitting

The SED for each SN is fitted with an elementary one-component homogeneous dust model. A more sophisticated model fitting would require additional data from other bands. The analysis follows the procedure described by Fox et al. (2010, 2011). The flux density coming from warm dust at one equilibrium temperature is given by the Planck function modified with the dust mass absorption coefficient, which is frequency dependent. Assuming an optically thin dust shell with $\Delta\, r/r \sim 1/10$, the flux is given by

$$F_\nu = \frac{M_{\rm d} B_\nu(T_{\rm d})\kappa_\nu(a)}{d^2}, \quad (1)$$

where B_ν ($T_{\rm d}$) is the Planck function, $\kappa_\nu(a)$ is the dust mass absorption coefficient as a function of the grain size a, $M_{\rm d}$ is the dust mass, and d is the distance of the source from the observer. The dust mass absorption coefficient is given by

$$\kappa_\nu(a) = \left(\frac{3}{4\pi\rho a^3}\right)(\pi a^2 Q_\nu(a)), \quad (2)$$

where ρ is the volume density of the dust and $Q_\nu(a)$ is the frequency dependent emission efficiency of the dust. $Q_\nu(a)$ is given in Figure 4 of Fox et al. (2010) and it is computed numerically. Because we only have two data points for each SN at each epoch, we are limited to using one temperature component and one dust composition. Fox et al. (2011) found that assuming a pure graphite dust population with $a = 0.1$ μm gives the best fitting coefficients. The distinction between a graphite and a silicate dust population is a spectral feature around 9 μm, which is not captured by our data. They also found that a silicate dust model resulted in higher temperatures, masses, and luminosities. In many cases, silicate grains require an improbably high luminosity from the SN to heat them up to the observed temperature. Thus, we assume a graphite dust population with a grain radius of 0.1 μm. We note here that at early time ($\lesssim$200 days), the SN light still dominates dust emission in mid-IR and the results from SED fitting in those epochs might not reflect dust properties accurately. We also note that the 3.6 μm band can be contaminated by the PAH emission while the 4.5 μm band can be contaminated by CO emission at 4.65 μm.

We fit Equation (1) to our data using the method `curve_fit` in `SciPy` package, which varies fitting parameters to find the best fit to the data using the method of least squares (Jones et al. 2001). The standard deviations of the fitting parameters are also computed by `curve_fit`. Table 3 shows best-fit temperatures and dust masses with corresponding uncertainties for all SNe for which data in both IRAC bands at the same epoch exist. Other epochs of observations where only one band is observed are presented in Table 4. We note that these uncertainties are small because they are derived solely from the photometric uncertainties. They do not reflect the errors due to our assumption that the dust emission is optically thin and the spectrum is a modified blackbody. The dust luminosity is computed by integrating Equation (1) at all frequencies using the fitted warm dust mass and temperature. We note that due to the lack of spectral information, we cannot rule out pre-existing dust and the best-fit dust masses reported here should be taken as an upper limit to the amount of newly formed dust. We also reiterate here that our observations are only sensitive to warm dust and there could be a large fraction of dust mass hiding at colder temperatures. We find that dust masses are between 10^{-6} and $10^{-2}\,M_\odot$, in agreement with previous works concluding that warm dust alone cannot account for all of the dust predicted to be produced in a CCSN. Figure 4 shows the time evolution of dust luminosity, temperature, and mass along with data on Type II-P SNe from Szalai & Vinkó (2013) and Type IIn SNe from Fox et al. (2011). The Type II-P events in

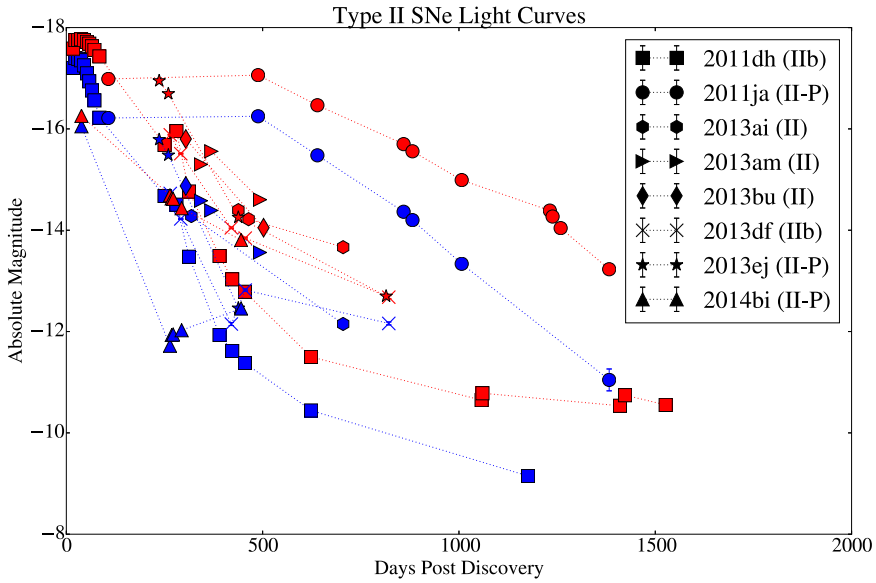

Figure 3. Collage of light curves of Type II SNe with photometry based on image subtraction. Red and blue markers represent [4.5] and [3.6], respectively. The error bars are smaller than the plotting symbols.

Szalai & Vinkó (2013) and SNe in our sample have dust luminosity, temperatures, and mass estimates in the same range. In comparison with Type IIn events with confirmed early CSM interactions that can heat pre-existing dusts to high temperatures, SNe in our sample have less luminous dust emission, and, at roughly the same temperature, less inferred dust mass.

In the plot showing warm dust mass (Figure 4), two dotted lines represent the predicted dust mass that has been processed by the forward shock from the SN, which is given by Equation (6) in Fox et al. (2011). Assuming a dust to gas ratio of 0.01, we get

$$M_{\rm d}\,(M_{\odot}) \approx 0.0028\left(\frac{v_{\rm s}}{15{,}000\ {\rm km\ s^{-1}}}\right)^{3}\left(\frac{t}{\rm year}\right)^{2}\left(\frac{a}{\mu{\rm m}}\right), \quad (3)$$

where $v_{\rm s}$ is the shock velocity, t is the time post explosion, and a is the grain size (assumed in this work to be 0.1 μm). The last panel in Figure 4 shows that, for almost all cases, the predicted shocked dust mass is much lower than the mass derived from our observations. As a result, shock heating of pre-existing dust is likely ruled out for all events within a year following the explosion. Even for later times, to invoke shock heating, we must assume a high shock velocity of 15,000 km s^{-1}.

The temporal evolution of the observed mass seems to show two different trends at about a year post explosion. Some of the events, such as SN 2011dh, SN 2013dk, and especially SN 2014bi, show a large decrease in the dust mass at this epoch. This could be a signature of either dust destruction or reduced CSM/shock interactions. Another group of SNe, especially SN 2011ja and SN 2014C, show an increase in the dust mass, which could be due to either the formation of new dust or an intensifying dust heating source. For SN 2011ja, both the dust luminosity and dust temperature are dropping while the warm dust mass is growing. This disfavors the fading dust heating source scenario. Next, we discuss case studies of some extreme SNe in our sample.

4. CASE STUDIES

4.1. SN 2011ja: A Type II-P with New Dust Formation in a Cold Dense Shell (CDS)

SN 2011ja is a Type II-P SN in the nearby galaxy NGC 4945 at a distance of 3.8 Mpc (Mould & Sakai 2008). It was discovered on 2011 December 18 by Monard et al. (2011) and the spectrum obtained a day later showed that it was a young Type II-P SN that shared similar spectral features with SN 2004et a week after maximum light (Milisavljevic et al. 2011). Chakraborti et al. (2013) obtained X-ray and radio observations in two epochs out to about 100 days. They found signatures of circumstellar interactions, which likely resulted from the fast moving ejecta colliding with the slower stellar wind from the progenitor before it exploded. They deduced from the observations that the progenitor was likely a red supergiant (RSG) with initial mass $M \gtrsim 12\,M_{\odot}$. Andrews et al. (2016) performed multi-band follow-up observations in the optical, near-IR, and mid-IR. The first 4 out of 10 epochs of the *Spitzer* observations used in this work were also presented in their paper. After 105 days, they observed a decrease in the optical flux, a rise in the near-IR flux, and an attenuation in the red-wing of Hα emission lines. These are strong indications that SN 2011ja is producing dust early on in the CDS created when the ejecta run into the CSM. The dust could not have formed in the inner ejecta, because the temperature would be too high at such an early epoch. Using a radiative transfer model to fit the SED, they inferred $\sim 10^{-5}$–$10^{-4}\,M_{\odot}$ of dust at 100 days, depending on the assumed geometry. By 857 days, at least $\sim(2.0\text{–}6.0) \times 10^{-4}\,M_{\odot}$ of dust has formed. They classified SN 2011ja with a growing group of Type II-P SNe, among them SN 2004dj and SN 2007od, which exhibit unusual evolution at late times due to the CSM interactions. This indicates that their progenitors lose enough mass before the SN explosion to create a dense CSM environment that is close enough for the forward shock to encounter within a few hundred days, but not so that CSM interactions commence immediately after explosion, as in the case of Type IIn SNe.

Table 3
Mid-IR Photometry and SED Fitting Results

MJD	Epochs (days)	$F_{[3.6]}$ (mJy)	$F_{[4.5]}$ (mJy)	r_s (cm)	r_{bb} (cm)	L_d ($L_\odot$)	M_d ($M_\odot$)	T_d (K)
				SN 2011dh (IIb)				
55730*	17	5.309(0.004)	4.87(0.01)	7.44×10^{14}	$8.45(0.15) \times 10^{15}$	$6.47(0.22) \times 10^{6}$	$7.10(0.11) \times 10^{-5}$	836(2)
55736*	23	6.344(0.006)	5.69(0.01)	9.96×10^{14}	$8.88(0.15) \times 10^{15}$	$7.93(0.26) \times 10^{6}$	$7.51(0.11) \times 10^{-5}$	858(2)
55743*	30	6.261(0.006)	5.71(0.01)	1.31×10^{15}	$9.07(0.16) \times 10^{15}$	$7.69(0.25) \times 10^{6}$	$8.08(0.12) \times 10^{-5}$	842(2)
55750*	37	6.104(0.006)	5.78(0.02)	1.62×10^{15}	$9.54(0.16) \times 10^{15}$	$7.25(0.23) \times 10^{6}$	$9.60(0.14) \times 10^{-5}$	809(2)
55758*	44	5.556(0.006)	5.70(0.01)	1.93×10^{15}	$1.04(0.02) \times 10^{16}$	$6.32(0.19) \times 10^{6}$	$1.32(0.02) \times 10^{-4}$	747(2)
55765*	52	4.808(0.005)	5.51(0.01)	2.27×10^{15}	$1.18(0.02) \times 10^{16}$	$5.43(0.16) \times 10^{6}$	$2.03(0.03) \times 10^{-4}$	676(1)
55771*	58	4.16(0.01)	5.33(0.01)	2.52×10^{15}	$1.35(0.02) \times 10^{16}$	$4.92(0.17) \times 10^{6}$	$3.10(0.06) \times 10^{-4}$	618(1)
55778*	65	3.52(0.01)	5.09(0.01)	2.81×10^{15}	$1.55(0.03) \times 10^{16}$	$4.58(0.16) \times 10^{6}$	$4.82(0.09) \times 10^{-4}$	565(1)
55785*	71	2.94(0.01)	4.77(0.01)	3.09×10^{15}	$1.77(0.03) \times 10^{16}$	$4.35(0.16) \times 10^{6}$	$7.18(0.14) \times 10^{-4}$	523(1)
55797*	84	2.145(0.008)	4.23(0.01)	3.64×10^{15}	$2.22(0.04) \times 10^{16}$	$4.25(0.16) \times 10^{6}$	$1.40(0.03) \times 10^{-3}$	464(1)
55963*	250	0.517(0.003)	0.845(0.004)	1.08×10^{16}	$7.52(0.22) \times 10^{15}$	$7.73(0.42) \times 10^{5}$	$1.31(0.04) \times 10^{-4}$	521(2)
55993*	280	0.441(0.004)	1.087(0.005)	1.21×10^{16}	$1.58(0.06) \times 10^{16}$	$1.33(0.10) \times 10^{6}$	$8.76(0.40) \times 10^{-4}$	412(2)
56026*	312	0.171(0.002)	0.363(0.002)	1.35×10^{16}	$7.24(0.32) \times 10^{15}$	$3.85(0.32) \times 10^{5}$	$1.60(0.08) \times 10^{-4}$	446(2)
56103*	390	0.0413(0.0008)	0.112(0.001)	1.69×10^{16}	$5.92(0.47) \times 10^{15}$	$1.54(0.24) \times 10^{5}$	$1.35(0.13) \times 10^{-4}$	392(4)
56135*	422	0.0309(0.0007)	0.074(0.001)	1.82×10^{16}	$3.89(0.38) \times 10^{15}$	$8.68(1.63) \times 10^{4}$	$5.17(0.57) \times 10^{-5}$	419(5)
56168*	454	0.0248(0.0006)	0.0586(0.0009)	1.96×10^{16}	$3.43(0.38) \times 10^{15}$	$6.86(1.45) \times 10^{4}$	$3.98(0.49) \times 10^{-5}$	421(6)
56337*	623	0.0105(0.0004)	0.0179(0.0005)	2.69×10^{16}	$1.17(0.23) \times 10^{15}$	$1.67(0.63) \times 10^{4}$	$3.36(0.70) \times 10^{-6}$	505(14)
				SN 2011ja (II-P)				
56012*	106	5.88(0.02)	7.73(0.01)	4.62×10^{15}	$1.01(0.02) \times 10^{16}$	$2.57(0.08) \times 10^{6}$	$1.82(0.03) \times 10^{-4}$	606(1)
56393*	488	6.07(0.01)	8.29(0.02)	2.11×10^{16}	$1.10(0.01) \times 10^{16}$	$2.72(0.07) \times 10^{6}$	$2.27(0.03) \times 10^{-4}$	589(1)
56544*	639	2.98(0.01)	4.80(0.01)	2.76×10^{16}	$1.06(0.02) \times 10^{16}$	$1.59(0.05) \times 10^{6}$	$2.54(0.05) \times 10^{-4}$	526(1)
56764	859	1.07(0.02)	2.365(0.009)	3.71×10^{16}	$1.19(0.09) \times 10^{16}$	$9.45(1.35) \times 10^{5}$	$4.51(0.36) \times 10^{-4}$	435(4)
56787	881	0.92(0.02)	2.076(0.008)	3.81×10^{16}	$1.15(0.10) \times 10^{16}$	$8.46(1.37) \times 10^{5}$	$4.31(0.40) \times 10^{-4}$	430(5)
56912	1007	0.42(0.01)	1.23(0.01)	4.35×10^{16}	$1.35(0.13) \times 10^{16}$	$6.81(1.29) \times 10^{5}$	$7.55(0.87) \times 10^{-4}$	376(4)
57288	1382	0.05(0.01)	0.24(0.02)	5.97×10^{16}	$1.33(0.95) \times 10^{16}$	$2.91(4.06) \times 10^{5}$	$1.06(0.90) \times 10^{-3}$	306(24)
				SN 2013ai (II)				
57057	704	0.0099(0.0002)	0.0258(0.0003)	3.05×10^{16}	$6.02(0.51) \times 10^{15}$	$1.72(0.28) \times 10^{5}$	$1.34(0.13) \times 10^{-4}$	400(4)
				SN 2013am (II)				
56715	342	0.0550(0.0004)	0.0688(0.0005)	1.48×10^{16}	$4.36(0.24) \times 10^{15}$	$5.53(0.57) \times 10^{5}$	$3.14(0.16) \times 10^{-5}$	629(5)
56741	369	0.0461(0.0004)	0.0873(0.0006)	1.59×10^{16}	$8.83(0.40) \times 10^{15}$	$7.38(0.64) \times 10^{5}$	$2.13(0.11) \times 10^{-4}$	475(3)
56865	493	0.0215(0.0003)	0.0362(0.0004)	2.13×10^{16}	$4.80(0.34) \times 10^{15}$	$2.89(0.39) \times 10^{5}$	$5.56(0.42) \times 10^{-5}$	510(5)
				SN 2013bu (II)				
56707	304	0.1435(0.0007)	0.218(0.001)	1.31×10^{16}	$7.17(0.21) \times 10^{15}$	$8.50(0.47) \times 10^{5}$	$1.09(0.03) \times 10^{-4}$	546(2)
				SN 2013df (IIb)				
56715	264	0.0512(0.0004)	0.0963(0.0006)	1.14×10^{16}	$1.02(0.04) \times 10^{16}$	$9.93(0.82) \times 10^{5}$	$2.80(0.13) \times 10^{-4}$	477(2)
56741	291	0.0322(0.0003)	0.0684(0.0005)	1.26×10^{16}	$1.02(0.05) \times 10^{16}$	$7.67(0.76) \times 10^{5}$	$3.19(0.18) \times 10^{-4}$	446(3)
56870	420	0.0048(0.0001)	0.0177(0.0003)	1.82×10^{16}	$1.26(0.14) \times 10^{16}$	$3.96(0.83) \times 10^{5}$	$7.83(1.04) \times 10^{-4}$	340(4)
56906*	455	0.0088(0.0002)	0.0147(0.0002)	1.97×10^{16}	$3.31(0.37) \times 10^{15}$	$1.43(0.31) \times 10^{5}$	$2.60(0.30) \times 10^{-5}$	515(8)
57271	821	0.0048(0.0001)	0.0050(0.0001)	3.55×10^{16}	$1.03(0.22) \times 10^{15}$	$5.77(2.34) \times 10^{4}$	$1.32(0.25) \times 10^{-6}$	736(27)
				SN 2013dk (Ic)				
56733	268	0.1588(0.0007)	0.2021(0.0009)	1.16×10^{16}	$8.26(0.26) \times 10^{15}$	$1.89(0.11) \times 10^{6}$	$1.16(0.03) \times 10^{-4}$	621(3)
56734	269	0.1378(0.0007)	0.2040(0.0009)	1.16×10^{16}	$1.02(0.03) \times 10^{16}$	$1.85(0.11) \times 10^{6}$	$2.15(0.07) \times 10^{-4}$	556(2)
56758	292	0.1067(0.0006)	0.1528(0.0008)	1.27×10^{16}	$8.44(0.30) \times 10^{15}$	$1.39(0.09) \times 10^{6}$	$1.41(0.05) \times 10^{-4}$	569(3)
56763	298	0.1164(0.0006)	0.1440(0.0008)	1.29×10^{16}	$6.72(0.25) \times 10^{15}$	$1.36(0.10) \times 10^{6}$	$7.35(0.26) \times 10^{-5}$	635(3)
56894	428	0.0526(0.0004)	0.0620(0.0005)	1.85×10^{16}	$4.13(0.24) \times 10^{15}$	$6.03(0.66) \times 10^{5}$	$2.59(0.14) \times 10^{-5}$	660(6)
57109	644	0.0198(0.0003)	0.0133(0.0002)	2.78×10^{16}	$1.02(0.20) \times 10^{15}$	$5.11(1.84) \times 10^{5}$	$4.84(0.60) \times 10^{-7}$	1277(51)
				SN 2013ej (II-P)				
56734	236	0.778(0.002)	1.465(0.002)	1.02×10^{16}	$1.66(0.02) \times 10^{16}$	$2.65(0.06) \times 10^{6}$	$7.50(0.09) \times 10^{-4}$	477(1)
56758	259	0.587(0.001)	1.158(0.002)	1.12×10^{16}	$1.58(0.02) \times 10^{16}$	$2.16(0.05) \times 10^{6}$	$7.15(0.10) \times 10^{-4}$	464(1)
56936	438	0.0363(0.0004)	0.1224(0.0007)	1.89×10^{16}	$1.18(0.05) \times 10^{16}$	$4.13(0.32) \times 10^{5}$	$6.39(0.31) \times 10^{-4}$	355(1)
				SN 2014C (Ib)				
56707	45	4.560(0.004)	6.236(0.005)	1.96×10^{15}	$3.31(0.02) \times 10^{16}$	$2.44(0.03) \times 10^{7}$	$2.04(0.01) \times 10^{-3}$	588(1)

Table 3
(Continued)

MJD	Epochs (days)	$F_{[3.6]}$ (mJy)	$F_{[4.5]}$ (mJy)	r_s (cm)	r_{bb} (cm)	L_d ($L_\odot$)	M_d ($M_\odot$)	T_d (K)
56905	243	2.474(0.003)	3.134(0.004)	1.05×10^{16}	$2.12(0.02) \times 10^{16}$	$1.26(0.02) \times 10^{7}$	$7.52(0.06) \times 10^{-4}$	623(1)
56937	274	2.878(0.003)	3.527(0.004)	1.19×10^{16}	$2.15(0.02) \times 10^{16}$	$1.44(0.02) \times 10^{7}$	$7.40(0.05) \times 10^{-4}$	640(1)
57284	622	3.551(0.004)	5.076(0.005)	2.69×10^{16}	$3.18(0.02) \times 10^{16}$	$1.98(0.02) \times 10^{7}$	$1.99(0.01) \times 10^{-3}$	570(1)
57290	628	3.284(0.003)	4.476(0.004)	2.71×10^{16}	$2.79(0.02) \times 10^{16}$	$1.75(0.02) \times 10^{7}$	$1.45(0.01) \times 10^{-3}$	590(1)
57304	642	3.340(0.003)	5.227(0.005)	2.77×10^{16}	$3.66(0.02) \times 10^{16}$	$2.05(0.02) \times 10^{7}$	$2.95(0.02) \times 10^{-3}$	535(1)
57435	772	2.558(0.003)	4.214(0.004)	3.34×10^{16}	$3.54(0.02) \times 10^{16}$	$1.67(0.02) \times 10^{7}$	$2.93(0.02) \times 10^{-3}$	518(1)
57442	780	2.471(0.003)	4.165(0.004)	3.37×10^{16}	$3.63(0.02) \times 10^{16}$	$1.67(0.02) \times 10^{7}$	$3.17(0.02) \times 10^{-3}$	510(1)
57464	801	2.414(0.003)	4.179(0.004)	3.46×10^{16}	$3.78(0.03) \times 10^{16}$	$1.69(0.02) \times 10^{7}$	$3.55(0.02) \times 10^{-3}$	502(1)
				SN 2014L (Ic)				
56723	40	1.152(0.002)	1.234(0.002)	1.73×10^{15}	$1.37(0.02) \times 10^{16}$	$9.23(0.23) \times 10^{6}$	$2.44(0.03) \times 10^{-4}$	718(1)
56750	67	0.738(0.002)	1.095(0.002)	2.90×10^{15}	$1.99(0.03) \times 10^{16}$	$7.01(0.17) \times 10^{6}$	$8.23(0.11) \times 10^{-4}$	555(1)
56890	206	0.1874(0.0008)	0.348(0.001)	8.93×10^{15}	$1.55(0.04) \times 10^{16}$	$2.39(0.11) \times 10^{6}$	$6.43(0.16) \times 10^{-4}$	481(1)
				SN 2014bi (II-P)				
56847*	38	0.576(0.001)	0.450(0.001)	1.67×10^{15}	$3.83(0.11) \times 10^{15}$	$2.90(0.15) \times 10^{6}$	$1.04(0.02) \times 10^{-5}$	1015(5)
57072	264	0.0106(0.0002)	0.1060(0.0007)	1.14×10^{16}	$8.89(0.51) \times 10^{16}$	$4.94(0.55) \times 10^{6}$	$7.24(0.57) \times 10^{-2}$	241(1)
57076	268	0.0129(0.0002)	0.1003(0.0007)	1.16×10^{16}	$5.64(0.31) \times 10^{16}$	$2.70(0.29) \times 10^{6}$	$2.54(0.19) \times 10^{-2}$	260(1)
57080	272	0.0130(0.0002)	0.0996(0.0006)	1.18×10^{16}	$5.45(0.30) \times 10^{16}$	$2.59(0.27) \times 10^{6}$	$2.36(0.17) \times 10^{-2}$	261(1)
57102	293	0.0141(0.0002)	0.0840(0.0006)	1.27×10^{16}	$3.27(0.18) \times 10^{16}$	$1.30(0.14) \times 10^{6}$	$7.31(0.53) \times 10^{-3}$	284(1)
57253	445	0.0210(0.0003)	0.0470(0.0004)	1.92×10^{16}	$5.07(0.32) \times 10^{15}$	$1.67(0.20) \times 10^{5}$	$8.32(0.58) \times 10^{-5}$	432(3)

Note. A table of all epochs of observations with two simultaneous channels with image-subtraction photometry along with the dust parameters from SED fitting. All SN 2011dh data are from PID 70207(PI Helou) and the first three epochs of SN 2011ja are from PID 80239 and 90178 (PI Andrews). The fourth epoch of SN 2013df is from PID 10139 (PI Fox). The first epoch of SN 2014bi is from PID 10046 (PI Sanders). The rest are from SPIRITS, PID 10136, and 11063 (PI Kasliwal).

Table 4
Additional One-channel Mid-IR Photometry and Upper Limits

Name	MJD	$F_{[3.6]}$ (mJy)	$F_{[4.5]}$ (mJy)
2011dh	56771.17	…	0.0082(0.0002)
2011dh	56773.34	…	0.0093(0.0002)
2011dh	56889.65	0.0032(0.0001)	<0.018
2011dh	57123.57	…	0.0074(0.0002)
2011dh	57136.77	…	0.0089(0.0002)
2011dh	57240.05	…	0.0075(0.0002)
2011dh	57493.52	…	<0.0066
2011ja	57136.92	…	0.706(0.008)
2011ja	57143.95	…	0.634(0.007)
2011ja	57164.49	…	0.514(0.008)
2013ai	56670.92	0.0703(0.0005)	…
2013ai	56790.67	<0.021	0.0507(0.0005)
2013ai	56816.68	…	0.0430(0.0004)
2013ai	57168.89	<0.016	<0.013
2013am	57253.44	<0.020	<0.013
2013bu	56905.83	…	0.043(0.004)
2013bu	57284.82	<0.016	<0.013
2013df	57459.83	<0.022	<0.021
2013dk	57115.25	<0.025	<0.025
2013ej	57312.98	<0.0059	0.029(0.001)
2014L	57280.41	<0.027	<0.027
2014df	56929.54	0.162(0.001)	…
2014df	57331.12	<0.008	<0.007

Note. A table of additional photometry points from epochs with only one-channel detection. An upper limit in another channel is provided when the SN is observed with a non-detection. Finally, for each SN with image-subtraction photometry, we provide flux upper limits for the first epoch where the SN fades to non-detection. All limits are 9σ, while error bars are 1σ. All data come from SPIRITS, PID 10136, and 11063 (PI Kasliwal).

SN 2011ja has been observed 10 times with *Spitzer*. Seven epochs have concurrent coverage in both bands. Most notably, the light curve plateaus out to 500 days post explosion, then declines with the increasing [3.6]–[4.5] color. This photometric evolution is consistent with a warm dust mass that increases monotonically with time from $10^{-4}\,M_\odot$ at 107 days to $10^{-3}\,M_\odot$ at 1383 days. Consider the blackbody radius that serves as a lower limit for the size of the dust shell responsible for the thermal emission (e.g., Fox et al. 2011) in comparison with the shock radius. For every epoch of observations, we see that the shock radius, assuming the ejecta speed between 5000 and 15,000 km s^{-1}, is a factor of a few larger than the blackbody radius. The blackbody radius remains almost constant from 106 days to 1382 days, with $r_{bb} \approx 10^{16}$ cm while the shock radius assuming shock velocity of $v_s = 5000$ km s^{-1} evolves from 4.62×10^{15} cm to 5.97×10^{16} cm. This places the size lower limit of the emitting dust shell smaller than the shock radius in most epochs, even assuming the minimum shock velocity. This is consistent with the scenario proposed by Andrews et al. (2016) in which dust grains condense in the CDS between the forward and reverse shocks with the inner and outer circumstellar radii of at 4.5×10^{15} and 4.5×10^{16} cm, respectively. Since the blackbody radius only provides a lower limit of the location of the emitting dust, we cannot reject the scenario in which the dust emission comes from beyond the shock front, from pre-existing dust being radiatively heated by the CSM interaction. We note, as well, that for the highest velocity shock with $v_s = 15{,}000$ km s^{-1}, Figure 4 suggests that the dust mass seen could be explained by collisional heating of the pre-existing dust by the shock front. However, given the spectroscopic evidence of newly formed dust presented by Andrews et al. (2016), we conclude that at least some of the observed dust must be newly formed.

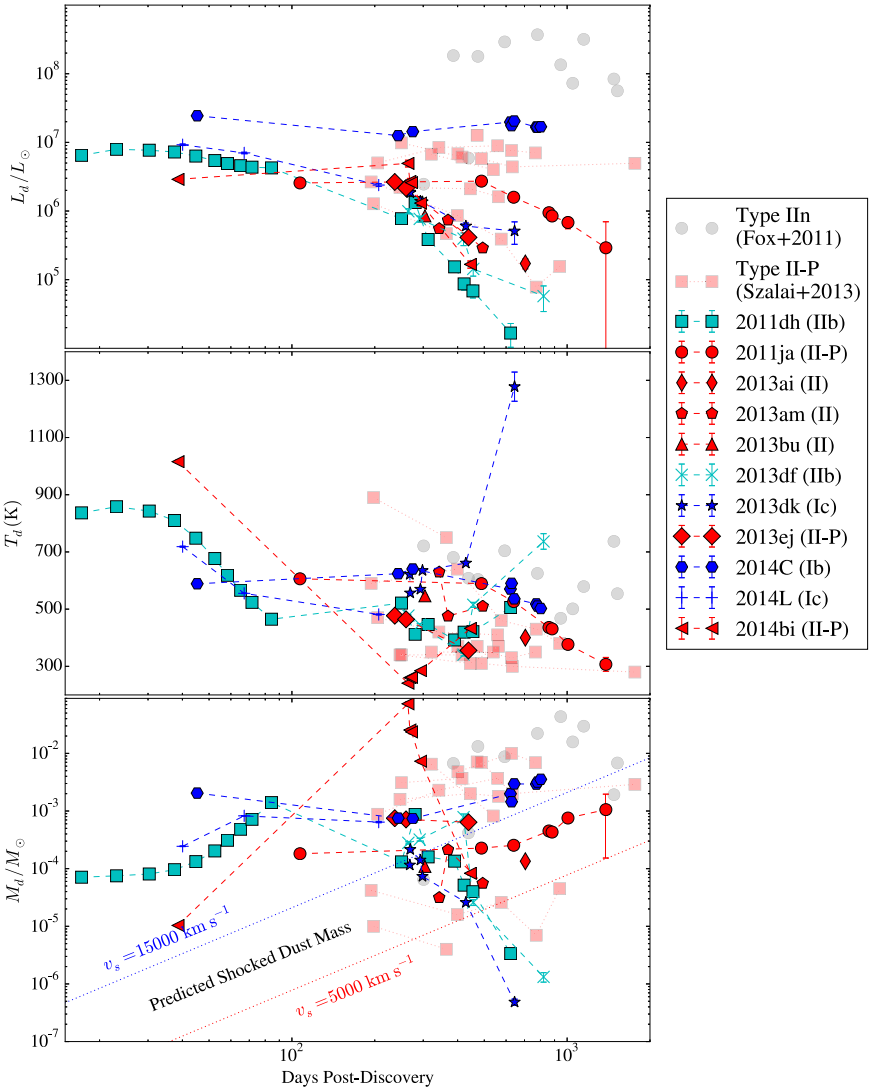

Figure 4. Time evolution of dust luminosity (top panel), temperature (middle panel), and mass (bottom panel) from fitting Equation (1) assuming 0.1 μm graphite grains. Overplotted (dotted line) on the warm dust mass evolution plot is the estimated dust mass assuming a shock heating scenario. The red points are Type II SNe, cyan points are Type IIb, and blue points are Type Ibc. Error bars (1σ) are plotted, but are smaller than the symbol size in most cases. The transparent grey circles are data for Type IIn SNe from Fox et al. (2011). The transparent red squares are data for Type II-P from Szalai & Vinkó (2013). Data points with connecting dotted lines represent the same SN with multiple epochs of data. No uncertainties are provided for these data points. This figure shows the diversity in temporal evolution of dust properties of CCSNe in our sample.

In comparison with other Type II events in our sample, SN 2011ja's early luminosity is very similar to that of SN 2011dh (IIb) in both channels. However, SN 2011ja's luminosity remains mostly constant out to 500 days, at which point it outshines every other SN in the sample. In comparison to the well-studied Type II-P SN 2004dj (Meikle et al. 2011; Szalai et al. 2011) and SN 2004et (Fabbri et al. 2011), SN 2011ja is more than a magnitude brighter than both of them, out to about 1000 days (see Figure 5). In terms of dust properties, SN 2004dj has $3.35 \times 10^{-5} M_\odot$ and $5.1 \times 10^{-5} M_\odot$ of warm dust at 859 days and 996 days, respectively (Szalai et al. 2011). For SN 2004et, Fabbri et al. (2011) used a more sophisticated clumpy dust model with an R^{-2} density distribution, a range of grain sizes from 0.1 to 1 μm, and a graphite to silicate ratio of 1:4. Their largest mass estimate is $\sim 10^{-3} M_\odot$ at 690 days. Szalai & Vinkó (2013), using a graphite dust model, reported a maximum dust mass of $10^{-2} M_\odot$ for SN 2006bp at 628 days. Most of the other Type II-P SNe in their sample produced around $5 \times 10^{-3} M_\odot$ of dust. The Type IIn SNe with strong CSM interactions tend to show more warm dust mass as shown in Figure 4. Fox et al. (2011, 2013) reported the typical dust mass, assuming graphite dust composition, of at most $2.2 \times 10^{-2} M_\odot$, with most of their sample having an observed dust mass of around $5 \times 10^{-3} M_\odot$. They concluded, as well, that most of the dust was pre-existing, and that the strong CSM interactions in Type IIn events are able to heat up more dust than in other events with weaker or no CSM interactions. We conclude that SN 2011ja stands out from other Type II events in our sample due to CSM interaction. In terms of the warm dust properties, it is not an outlier from the general population of interacting Type II-P SNe.

4.2. SN 2014C: An Interacting Stripped-envelope Supernova with a Possible LBV Progenitor

SN 2014C is an SN Ib in the nearby galaxy NGC 7331, discovered on 2014 January 5. It was classified as a young SN Ib with a spectrum matching that of SN 1999ex at 6 days before

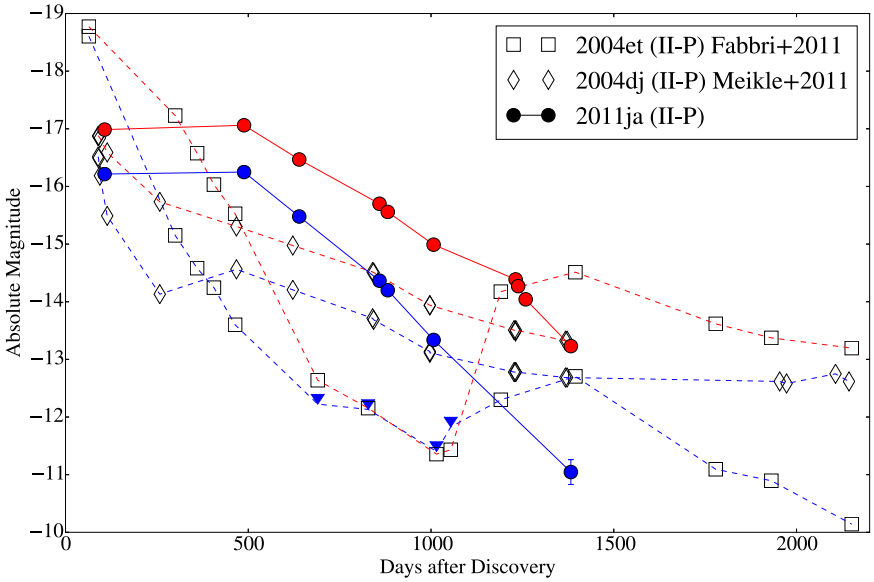

Figure 5. Light curve of SN 2011ja in both IRAC channels, in comparison with that of SN 2004et (Fabbri et al. 2011) and SN 2004dj (Meikle et al. 2011; Szalai et al. 2011). SN 2004et was not detected in the 3.6 μm band from around 700 to 1100 days. The four downward arrows in the light curve of SN 2004et indicate the 3σ detection limits.

maximum light (Kim et al. 2014). The velocities of He and Si absorption features are measured to be about 13,800 km s^{-1} and 9900 km s^{-1}, respectively. SN 2014C was observed with the Very Large Array (VLA) on 2014 January 11 to have a flux of 0.80 $\pm$ 0.04 mJy at 7 GHz (Kamble et al. 2014). It was detected by the Combined Array for Research in Millimeter Astronomy (CARMA; Bock et al. 2006) on 2014 January 13 at a flux level of 1.2 $\pm$ 0.2 mJy in 85 GHz waveband (Zauderer et al. 2014). Milisavljevic et al. (2015) analyzed optical spectra of SN 2014C and reported a remarkable metamorphosis of this SN from a typical Type Ib to an interacting Type IIn. This is similar to the case of SN 2001em that underwent a similar transition from Type Ibc to Type IIn when Hα, X-ray, and radio emissions were detected $\sim$2.5 years post explosion (Chugai & Chevalier 2006). Nonetheless, SN 2014C was the first example of this transition being caught in action with frequent observations during the transition. The onset of Hα emission with intermediate line width along with an X-ray detection by *Chandra* and the aforementioned radio emission are strong evidence of CSM interaction with a dense H-rich shell. The observations placed the shell radius at $\gtrsim 3 \times 10^{16}$ cm. Milisavljevic et al. (2015) constrained the density of the unshocked CSM by the relative strength of the narrow lines in the spectra. The absence of a [O II] line in the presence of [O III] lines set a lower limit on the density of 10^4 cm^{-3}. The relative strengths of the [Fe VII] lines sets the upper limit of the density at 10^7 cm^{-3}. Furthermore, the width of the unresolved [O III] line indicates that the CSM velocity is less than 100 km s^{-1}. Optical spectra presented by Milisavljevic et al. (2015) do not show a blueshifted line profile, as may be expected in case of new dust being formed in the ejecta behind the shock front (assuming spherical symmetry). If the geometry of the CSM is disk-like and not being viewed edge-on, CSM dust will not produce a blueshifted line profile. The earliest signature of CSM interactions observed from the ground came 113 days post explosion when the SN emerged from behind the Sun. The only observation carried out before this gap was on 2014 January 9, four days before maximum in V band. The gap in ground-based observations is filled in with *Spitzer* observations presented here.

SN 2014C was observed in nine epochs with *Spitzer*, with the first epoch at 45 days while the SN was behind the Sun for ground-based observers. The light curves in both channels were rising from $\sim$250 days until the latest epoch at 801 days. Figure 6 shows the time evolution of the SED of SN 2014C along with concurrent NIR follow-up photometry at 274 days and 628 days post explosion. The NIR fluxes indicate that the hot component of the SN has already faded, especially at 628 days, and the SED is dominated by warm dust emissions in the mid-IR. Fluxes in both IRAC bands rise between 243 days and 622 days. The SEDs from the last three epochs from 772 to 801 days are almost identical. While this re-brightening in mid-IR has been observed in a number of other events, even in some Type Ia with CSM interactions (see SN 2005gj and SN 2002ic; Fox et al. 2013), it has rarely been observed directly in a stripped-envelope CCSN. (One such case was Type Ibn SN 2006jc (Smith et al. 2008) where dust formed in the post-shock gas at 50–100 days after discovery.) Multiple mechanisms could cause an SN to re-brighten in mid-IR at late times. In Type II SNe, such as SN 2004dj and SN 2004et discussed earlier, the re-brightening can also be attributed to new dust being formed in either the SN ejecta or the CDS behind the shock. However, due to the lack of dust attenuation in optical spectral lines, this scenario is unlikely. In the cases of Type Ia-CSM events where dust production is not expected, Fox et al. (2013) showed that the re-brightening can be attributed to a pre-existing dust shell being radiatively heated by optical and X-ray photons from CSM interactions. Another possible scenario is the collisional heating of pre-existing dust by the forward shock. Next, we consider these last two shock heating mechanisms.

Assuming a gas-to-dust mass ratio of 100 and that the dust sputtering timescales are significantly shorter than the cooling timescale of the shocked CSM, Figure 4 shows that the observed dust mass of SN 2014C is consistently higher than the predicted CSM mass heated by a 15,000 km s^{-1} shock. Notably, the blackbody radius, which gives the lower limit

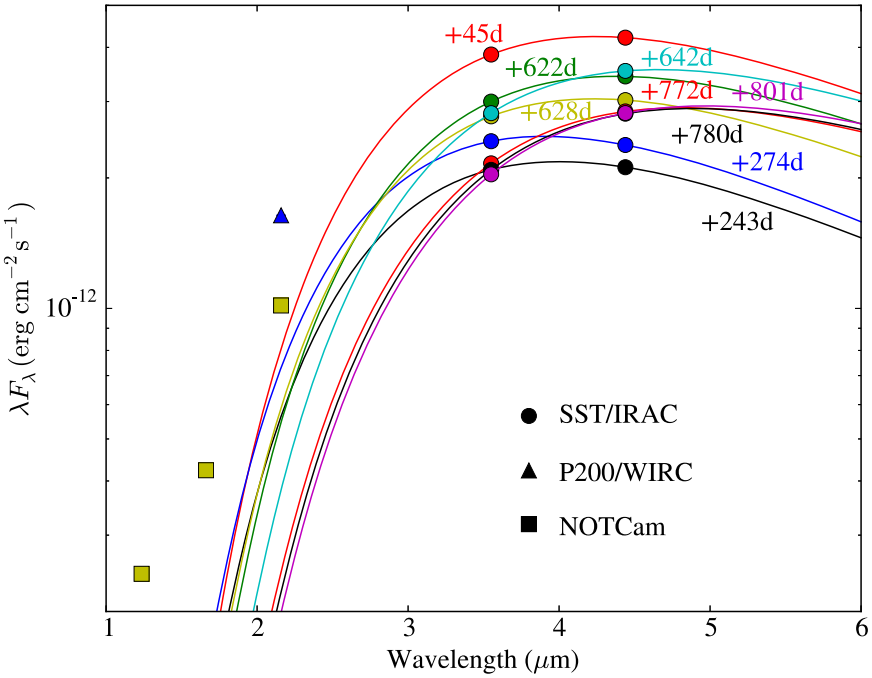

Figure 6. SED of SN 2014C ranging from 45 to 642 days post explosion. *Spitzer*/IRAC data are plotted in circles. Near-IR follow-up observations obtained at the Nordic Optical Telescope Near-Infrared Camera and Spectrograph (NOTCam) are plotted in squares, and the data obtained using the Wide-field InfraRed Camera (WIRC) on the 200 inch Telescope at Palomar Observatory are plotted in triangles. The overplotted lines are the best fit of Equation (1) using only mid-IR data.

for the dust shell size (e.g., Fox et al. 2011), is a factor of five larger than the shock radius, assuming a shock velocity of $v_s = 15{,}000\,\mathrm{km\,s^{-1}}$ at +45 days. This is an indication that, at least for this earliest epoch, the observed mid-IR flux is likely due to pre-existing dust radiatively heated by CSM interactions. This requires that SN 2014C starts to interact with the environment as early as 45 days post explosion. However, there are no X-ray observations at that epoch to confirm the CSM interactions. Milisavljevic et al. (2015) reported an X-ray luminosity of $1.3 \times 10^7\,L_\odot$ at 373 days, which can provide the dust luminosity observed around the same epochs.

We can estimate the CSM density by making a simple assumption about the geometry for this scenario. At the 45 day epoch, the site of interaction is at the shock radius $r_s = (2\text{–}6) \times 10^{15}\,\mathrm{cm}$, assuming shock velocities of $v_s = 5000\text{–}15{,}000\,\mathrm{km\,s^{-1}}$. The number density of hydrogen in the CSM can be approximated by

$$n_\mathrm{H} = \frac{3M_\mathrm{d}}{4\pi\left((r_\mathrm{s}+r_\mathrm{d})^3 - r_\mathrm{s}^3\right)}\frac{\chi}{m_\mathrm{H}}, \quad (4)$$

where r_d is the radial thickness of the mid-IR emitting dust and χ is the gas-to-dust mass ratio for which we adopt a value of 100. The thickness r_d can be approximated, assuming the dust in the CSM is in thermal equilibrium with the incident radiation from the shock at a temperature of 550 K (the mean inferred dust temperature over all epochs). We assume that the CSM is optically thin and composed of a uniform distribution of 0.1 μm sized amorphous carbon-type grains, where 0.1 μm is representative of the peak of the Mathis et al. (1977) grain size distribution. The approximate distance at which 0.1 μm carbonaceous grains are in thermal equilibrium with optical and UV photons of luminosity $\sim 10^7\,L_\odot$ (Milisavljevic et al. 2015; this work) is $r_d \sim 6 \times 10^{16}\,\mathrm{cm}$, consistent within a factor of two of the blackbody radius. From Equation (4), we therefore derive a gas number density of $n_\mathrm{H} \sim 3 \times 10^5\,\mathrm{cm^{-3}}$. This is consistent with the limits of 10^4–$10^7\,\mathrm{cm^{-3}}$ independently derived by Milisavljevic et al. (2015). We note that the range of assumed shock velocities does not significantly affect n_H, since $r_\mathrm{d} \gg r_S$ at 45 days. Furthermore, taking the velocity of the CSM of $100\,\mathrm{km\,s^{-1}}$ to be constant, and the blackbody radius as an approximate size of the CSM shell, this material must have been ejected from the progenitor of SN 2014C at least 100 years before the explosion.

Milisavljevic et al. (2015) proposed three possible origins for the CSM shell around SN 2014C: a short-lived Wolf–Rayet (WR) phase that swept up a slower RSG wind, a single eruptive ejection from a luminous blue variable (LBV) or binary interaction, or externally influenced CSM confinement. All of these scenarios require a brief (10^3 year) phase after the hydrogen envelope has been stripped. Although a thorough analysis of each scenario is beyond the scope of this paper, we present brief discussions on the implications of our results on the binary interaction and LBV eruption scenarios.

A possible origin for the dense dusty CSM of SN 2014C is an outflow from a massive binary formed as the result of non-conservative mass transfer during a brief Roche-lobe overflow phase (Vanbeveren et al. 1998). Such an event is thought to produce stripped-envelope WRs and is claimed to be occurring in interacting binary systems, such as NaSt1 (e.g., Crowther & Smith 1999; Mauerhan et al. 2015) and RY Scuti (Smith et al. 2011). Both systems host a WR-like star surrounded by a dusty, hydrogen-rich shell and may therefore be an example of a possible SN 2014C progenitor. The dust formation efficiency and mass-loss properties from massive binaries during non-conservative mass transfer are, however, unclear due to the paucity of observations of these systems.

We now consider the LBV eruption scenario. LBV nebulae exhibit outflow velocities of $\sim 100\,\mathrm{km\,s^{-1}}$ (Smith 2014), which are consistent with the observational constraints on the CSM

velocity ($\lesssim$100 km s^{-1}; Milisavljevic et al. 2015) and imply a dynamical timescale of $\lesssim$100 years given the inferred CSM blackbody radius. This timescale agrees with the observed ~1–10 year eruptive phases of LBVs. Given the inferred dust mass of the CSM ($2 \times 10^{-3}\,M_{\odot}$) and assuming a gas-to-dust mass ratio of 100, the implied mass-loss rate during the formation of the CSM is therefore $\gtrsim 2 \times 10^{-2}\,M_{\odot}\,\mathrm{yr}^{-1}$ and consistent with observed and predicted LBV mass-loss rates (Smith & Owocki 2006; Kochanek 2011). Observations of dusty LBV nebulae typically reveal $\gtrsim$0.01 $M_{\odot}$ (Smith & Owocki 2006) of dust; however, we note that several LBV nebulae, such as G24.73+0.69, HD 168625, and Hen 3-519, exhibit dust masses similar to that of the CSM (0.003–0.007 $M_{\odot}$; Smith et al. 1994; Clark et al. 2003; O'Hara et al. 2003). The consistency between mass-loss properties of an LBV outburst and the measured dust mass and radius of the CSM point to a single LBV-like eruption roughly 100 years pre-explosion as a plausible origin of the CSM shell around SN 2014C.

We conclude that the *Spitzer* observations of SN 2014C are consistent with dust being heated by optical/X-ray photons from an ongoing interaction between the SN shock and a CSM that originated from a LBV-like eruption.

4.3. SN 2014bi: The Extremely Low Color Temperature

SN 2014bi is a low-luminosity Type II-P SN detected in the galaxy NGC 4096, 11.3 Mpc away, on 2014 May 31 (Kumar et al. 2014). At the first epoch, 39 days post explosion, the SED is still dominated by the SN light. SN 2014bi is about 1.5 mag dimmer than SN 2011dh at the same epoch in both channels with a smaller [3.6]–[4.5] color of 0.2 mag. However, 200 days later, SN 2014bi becomes a very red source with [3.6]–[4.5] = 2.97 mag. This color temperature is associated with a low blackbody temperature of around 200 K. The warm dust mass calculated for this event is about $7.24 \times 10^{-2}\,M_{\odot}$ at 264 days, which is relatively high in comparison to dust masses for other CCSNe. However, the dust mass drops sharply to $2.54 \times 10^{-2}\,M_{\odot}$ only 4 days later. And by 293 days, the dust mass drops further to $7.31 \times 10^{-3}\,M_{\odot}$, an order of magnitude lower than that in the second epoch. At 445 days, the warm dust is almost gone, with a residual value of only $8.32 \times 10^{-5}\,M_{\odot}$. During this period, the apparent color temperature also increases to 423 K.

There are a number of possible causes for this drop in warm dust mass. First, this could be a signature of the SN shock that overtakes and destroys the dust shell. If the existing dust was being destroyed by a shock, then it would need to heat up before being destroyed, consistent with the observed small increase in color temperature. If we assume this scenario, we can calculate the density of the dust shell. To get an upper limit of the density, we assume a slow shock velocity of v_s = 5000 km s^{-1}. Assuming a grain size of 0.1 μm as before and and a grain density of 2 g cm^{-3}, the number density of dust particles needed to account for the observed decline in mass is only 3×10^{-2} cm^{-3}, which is very low, considering the typical density of a dust shell ~10^5 cm^{-3}. Second, another possible explanation is that the radiative heating source, e.g., emission from CSM interactions, is fading; thus, the amount of heated dust decreases. Finally, due to the lack of data at shorter wavelengths, it is also possible that a hotter component of the SN has cooled down and started to emit more significantly in the 3.6 μm band. In this case, the SED fit will underestimate the dust mass. We emphasize again that the 3.6 μm band can be contaminated by the PAH emission while the 4.5 μm band can be contaminated by CO emission at 4.65 μm. If *Spitzer* has still been cold, the IRS spectroscopy could have elucidated the nature of this SN.

4.4. Supernovae with Long-lived Infrared Emission Decades After Explosion

We detect IR emission from SN 1974E (II), SN 1979C (II-L), SN 1980K (II-L), SN 1986J (IIn), and SN 1993J (IIb), more than 20 years after explosion. The extended light curves for SN 1993J and SN 1979C in Figure 7 show that the luminosity for both events is still declining. This indicates that we are still detecting the light associated with the SNe and not just a constant background source, the remnant, or the companions of the progenitors of those SNe. The notable features of these old SNe are that they have a color of [3.6]–[4.5] $\approx$ 1 mag, and that the evolution is very slow. SN 1993J faded by $\approx$1 mag over the course of a decade, while the older SN 1979C evolved even more slowly, fading only by $\approx$0.2 mag over a decade. For other events without enough epochs of data to construct good light curves, we present the image-subtraction thumbnails that show that the SN has at least decayed from the reference epoch in Figure 8. From the thumbnails, one can appreciate the importance of image subtraction. In most cases, it is not possible to determine from the science frames alone whether or not we have a detection. Even in cases where there is an obvious source at the location of the SN, it is still difficult to differentiate between the SN light and the surrounding contribution. Image subtraction using a baseline of almost a decade as used in this work uncovers a number of old SNe that have never been reported to have late-time mid-IR emission previously (see Table 1 in Fox et al. 2011).

5. CONCLUSION

We have presented a systematic study of the general population of nearby supernovae that are hosted by galaxies in the SPitzer InfraRed Intensive Transient Survey (SPIRITS). The main results are threefold: (1) the detection statistics for the whole SN sample; (2) light curves for CCSNe and time evolution of dust parameters associated with each event; and (3) detailed case studies of several unusual events.

The detection statistics were obtained by visually vetting all observations of all SNe in the SPIRITS footprint. The results show that Type Ia SNe fade away much more quickly than Type Ib/c and Type II core-collapse SNe, with none of the Type Ia living past three years, unless they have CSM interactions. Type II SNe, on the other hand, tend to live for a very long time with 10 events living longer than three years. Five of those events, SN 1974E (II), SN 1979C (II-L), SN 1980K (II-L), SN 1986J (IIn), and SN 1993J (IIb), were detected decades after the explosion, providing the first sample of mid-IR observation of CCSNe at such late epochs. Other earlier surveys of SNe in the *Spitzer* archive missed these events because image subtraction was not done to reveal the subtle time evolution underneath the bright galaxy background.

We have created light curves collages for Type Ib/c and II SNe that have pre-explosion reference images using image subtraction based photometry. The light curves are heterogeneous compared to the light curves of Type Ia events. The

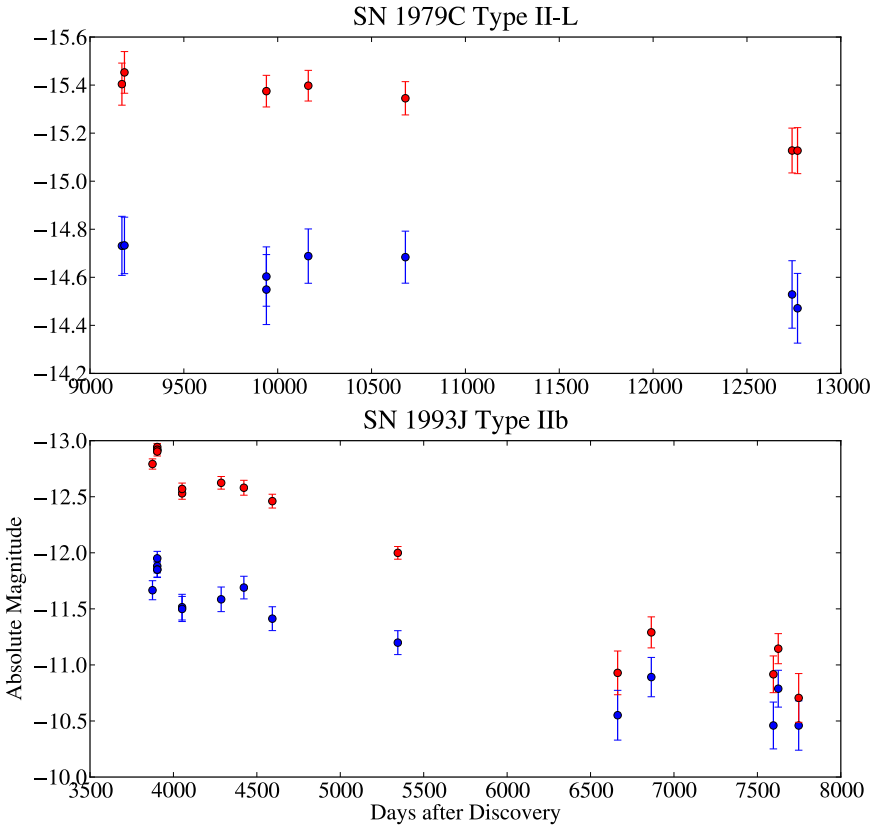

Figure 7. Two light curves show the very late time evolution of SN 1979C (top) and SN 1993J (bottom). The data are aperture photometry from the science frames, so the background contribution has not been fully subtracted out. For SN 1993J, the background emissions is minimal. For SN 1979C, the photometry is affected by association with a cluster. The SN light alone indeed was not as bright as [4.5] ~ -15 mag at such late epochs.

SEDs of the events with image-subtraction based photometry of both IRAC channels at the same epoch have been fitted with an elementary dust model with graphite grains of radius 0.1 μm at a single temperature. Luminosity, temperature, and warm dust mass were obtained from the fit. Our observations are only sensitive to warm dust and there could be more cold dust in these SNe that we could not detect. The light curves and temporal evolution of the dust parameters reveal some outliers from the general norm. An outlier among the Type Ib/c SNe is SN 2014C, which re-brightens around 260d post explosion with increasing observed dust mass. The lack of signatures for dust formation in the optical spectra (Milisavljevic et al. 2015) suggests that the emission in this SN comes from pre-existing dust. The blackbody radius at the first epoch suggests that the dust shell is heated by emission from CSM interaction. From the dust mass and blackbody radius, we obtain an estimate for the gas density of $\sim 10^6$ cm^{-3}, which is consistent with an LBV origin.

The majority of the hydrogen-rich Type II SNe' light curves loosely follow that of SN 2011dh, a well-observed Type IIb SN. We identify two interesting outliers. SN 2011ja (II-P) is over-luminous at 1000 days post-discovery. The temporal evolution of its dust parameters seem to suggest either an episode of dust production near the shock front or radiative heating of pre-existing dust by CSM interactions. The location of the emission at $\sim 10^{16}$ cm agrees with the location of new dust formation in the CDS model proposed by Andrews et al. (2016). SN 2014bi (II-P), on the other hand, is under-luminous and has a very low color temperature. The evolution of its dust parameters is opposite of that of other events, suggesting either dust destruction or dust heating with fading source. The dust mass determined for all events agree with the consensus that core-collapse SNe only produce 10^{-6} to $10^{-2}\,M_\odot$ of dust at early times. Few studies of late-time emission from cold dust ($\sim$10 K) show promising signs that the amount of dust required for CCSNe to contribute significantly to the cosmic dust content could be formed later on in their evolution (e.g., Barlow et al. 2010; Gomez et al. 2012; Indebetouw et al. 2014; Lau et al. 2015).

This work demonstrates the power of multi-epoch mid-IR observations as a tool for studying the diversity in evolution of CCSNe. Future wide-field IR surveys that have no biases in pre-selecting SN types could capture more events with shorter cadence, allowing for an even better statistical sample for a systematic study. This, accompanied by IR spectroscopic follow-up observations enabled by the *James Webb Space Telescope*, would further our understanding of the physics of CCSNe.

This work made use of observations from the *Spitzer Space Telescope* operated by the Jet Propulsion Laboratory, California Institute of Technology, under a contract with NASA. We acknowledge the use of some data from PIDs 70207 (PI Helou); 80239 and 90178 (PI Andrews); 10139 (PI Fox); and 10046 (PI Sanders). Ground-based observations presented were obtained at the Palomar Observatory, operated by California Institute of Technology. The Mount Lemmon Observing Facility is operated by the University of Minnesota. The Nordic Optical Telescope is operated by the Nordic Optical Telescope Scientific Association at the Observatorio del Roque de los Muchachos, La Palma, Spain, of the Instituto de

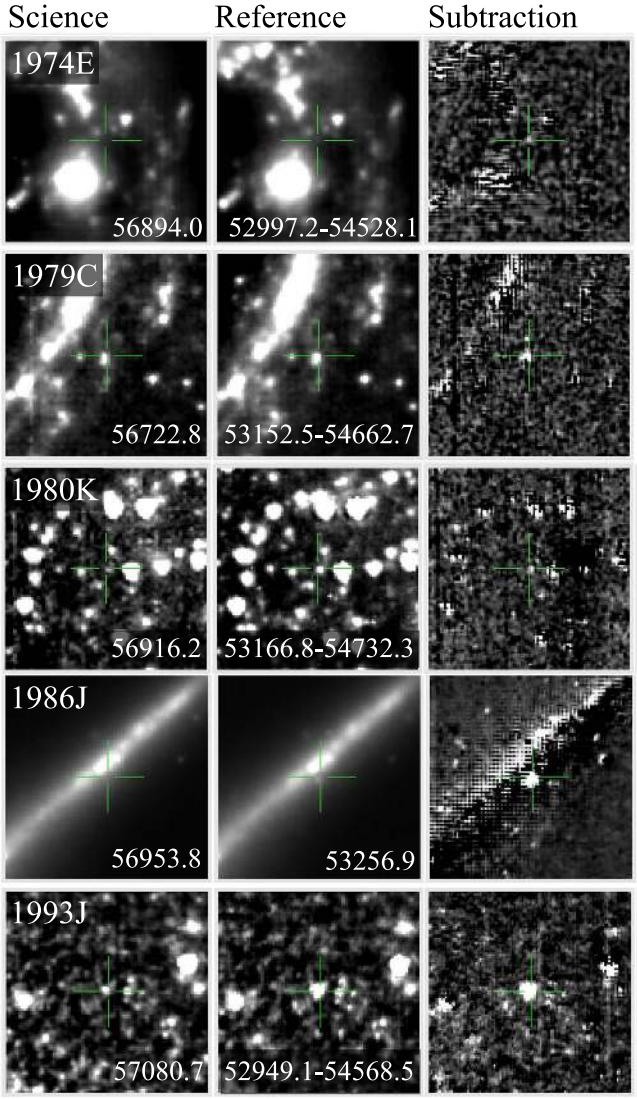

Figure 8. Image subtractions of five old Type II SNe showing the decrease in flux in the science frames taken at the later epochs compared to the references. From top to bottom, SN 1974E (II), SN 1979C (II-L), SN 1980K (II-L), SN 1986J (IIn), and SN 1993J (IIb). The MJD of each observation is shown on top of the image. In most cases, the references are stacks of *Spitzer* observations over the MJD ranges shown.

Astrofisica de Canarias. We are grateful for support from the NASA Spitzer mission grants to the SPIRITS program (PIDs 10136 & 11063). This research made use of Astropy, a community-developed core Python package for Astronomy Astropy Collaboration et al. (2013). We thank the anonymous referee for comments and suggestions. S.T. thanks Bill Scanlon for a close read of the manuscript. S.T. was supported by the Royal Thai Scholarship and a portion of this work was done while under the Claremont-Carnegie Astrophysics Research Program. R.D.G. was supported by NASA and the United States Air Force.

REFERENCES

Abbott, T. M., Aspin, C., Sorensen, A. N., et al. 2000, Proc. SPIE, 4008, 714
Adams, S. M., & Kochanek, C. S. 2015, MNRAS, 452, 2195
Andrews, J. E., Gallagher, J. S., Clayton, G. C., et al. 2010, ApJ, 715, 541
Andrews, J. E., Krafton, K. M., Ayani, K., et al. 2016, MNRAS, 457, 3241
Andrews, J. E., Sugerman, B. E. K., Clayton, G. C., et al. 2011, ApJ, 731, 47
Astropy Collaboration, Robitaille, T. P., Tollerud, E. J., et al. 2013, A&A, 558, A33
Ayani, K., Hashimoto, T., & Yamaoka, H. 2003, IAUC, 8048, 2
Barlow, M. J., Krause, O., Swinyard, B. M., et al. 2010, A&A, 518, L138
Bianco, F. B., Modjaz, M., Hicken, M., et al. 2014, ApJS, 213, 19
Bock, D. C.-J., Bolatto, A. D., Hawkins, D. W., et al. 2006, Proc. SPIE, 6267, 626713
Bose, S., Sutaria, F., Kumar, B., et al. 2015, ApJ, 806, 160
Bouchet, P., & Danziger, J. 2014, in IAU Symp. 296, ed. A. Ray & R. A. McCray, 9
Brown, R. L., Wild, W., & Cunningham, C. 2004, AdSpR, 34, 555
Cameron, E. 2011, PASA, 28, 128
Cappellaro, E., & Turatto, M. 1986, IAUC, 4262, 3
Chakraborti, S., Ray, A., Smith, R., et al. 2013, ApJ, 774, 30
Cherchneff, I. 2014, arXiv:1405.1216
Chugai, N. N., & Chevalier, R. A. 2006, ApJ, 641, 1051
Clark, J. S., Egan, M. P., Crowther, P. A., et al. 2003, A&A, 412, 185
Conseil, E., Fraser, M., Inserra, C., et al. 2013, CBET, 3431, 1
Cortini, G., Brimacombe, J., Tomasella, L., et al. 2013, CBET, 3597, 1
Crowther, P. A., & Smith, L. J. 1999, MNRAS, 308, 82
Diamond, T. R., Hoeflich, P., & Gerardy, C. L. 2015, ApJ, 806, 107
Duszanowicz, G., Joubert, N., Lee, N., et al. 2006, IAUC, 8771, 1
Dwek, E. 1983, ApJ, 274, 175
Dwek, E., & Arendt, R. G. 2015, ApJ, 810, 75
Dwek, E., A'Hearn, M. F., Becklin, E. E., et al. 1983, ApJ, 274, 168
Elias-Rosa, N., Pastorello, A., Maund, J. R., et al. 2013, MNRAS, 436, L109
Elias-Rosa, N., Van Dyk, S. D., Li, W., et al. 2011, ApJ, 742, 6
Ergon, M., Jerkstrand, A., Sollerman, J., et al. 2015, A&A, 580, A142
Fabbri, J., Otsuka, M., Barlow, M. J., et al. 2011, MNRAS, 418, 1285
Fazio, G. G., Hora, J. L., Allen, L. E., et al. 2004, ApJS, 154, 10
Filippenko, A. V. 1997, ARA&A, 35, 309
Filippenko, A. V., & Foley, R. J. 2005, IAUC, 8486, 3
Filippenko, A. V., Li, W. D., & Modjaz, M. 1999, IAUC, 7152, 2
Filippenko, A. V., Matheson, T., & Ho, L. C. 1993, ApJL, 415, L103
Foley, R. J., Smith, N., Ganeshalingam, M., et al. 2007, ApJL, 657, L105
Foley, R. J., Wong, D. S., Moore, M., & Filippenko, A. V. 2004, IAUC, 8353
Fox, O. D., Chevalier, R. A., Dwek, E., et al. 2010, ApJ, 725, 1768
Fox, O. D., Chevalier, R. A., Skrutskie, M. F., et al. 2011, ApJ, 741, 7
Fox, O. D., & Filippenko, A. V. 2013, ApJL, 772, L6
Fox, O. D., Filippenko, A. V., Skrutskie, M. F., et al. 2013, AJ, 146, 2
Fox, O. D., Johansson, J., Kasliwal, M., et al. 2016, ApJL, 816, L13
Gall, C., Hjorth, J., & Andersen, A. C. 2011, A&ARv, 19, 43
Gall, C., Hjorth, J., Watson, D., et al. 2014, Natur, 511, 326
Gehrz, R. D., & Ney, E. P. 1990, PNAS, 87, 4354
Gehrz, R. D., Roellig, T. L., Werner, M. W., et al. 2007, RSciI, 78, 011302
Gerardy, C. L. 2002, PhD thesis, Dartmouth College
Gomez, H. L., Krause, O., Barlow, M. J., et al. 2012, ApJ, 760, 96
Helou, G., Kasliwal, M. M., Ofek, E. O., et al. 2013, ApJL, 778, L19
Indebetouw, R., Matsuura, M., Dwek, E., et al. 2014, ApJL, 782, L2
Itagaki, K., Noguchi, T., Nakano, S., et al. 2013, CBET, 3498, 1
Jencson, J. E., Kasliwal, M. M., Johansson, J., et al. 2016, arXiv:1609.04444
Johansson, J., Goobar, A., Kasliwal, M. M., et al. 2014, arXiv:1411.3332
Jones, E., Oliphant, T., Peterson, P., et al. 2001, SciPy: Open source scientific tools for Python, [Online; accessed 2015-05-01]
Kamble, A., Soderberg, A., Zauderer, B. A., et al. 2014, ATel, 5763, 1
Kankare, E., Fraser, M., Ryder, S., et al. 2014, A&A, 572, A75
Kim, M., Zheng, W., Li, W., et al. 2014, CBET, 3777, 1
Kochanek, C. S. 2011, ApJ, 743, 73
Kochanek, C. S., Szczygieł, D. M., & Stanek, K. Z. 2012, ApJ, 758, 142
Kotak, R., Meikle, P., Pozzo, M., et al. 2006, ApJL, 651, L117
Kotak, R., Meikle, W. P. S., Farrah, D., et al. 2009, ApJ, 704, 306
Kumar, S., Zheng, W., Filippenko, A. V., et al. 2014, CBET, 3892, 1
Lau, R. M., Herter, T. L., Morris, M. R., Li, Z., & Adams, J. D. 2015, Sci, 348, 413
Lauroesch, J. T., Crotts, A. P. S., Meiring, J., et al. 2006, CBET, 421, 1
Low, F. J., Rieke, G. H., & Gehrz, R. D. 2007, ARA&A, 45, 43
Marion, G. H., Kirshner, R. P., Foley, R. J., Challis, P., & Irwin, J. 2012a, CBET, 3111, 3
Marion, G. H., Milisavljevic, D., & Irwin, J. 2012b, CBET, 3105, 2
Mathis, J. S., Rumpl, W., & Nordsieck, K. H. 1977, ApJ, 217, 425
Matsuura, M., Dwek, E., Barlow, M. J., et al. 2015, ApJ, 800, 50
Mattila, S., Meikle, W. P. S., Lundqvist, P., et al. 2008, MNRAS, 389, 141
Mauerhan, J., Smith, N., Van Dyk, S. D., et al. 2015, MNRAS, 450, 2551
Maxwell, A. J., Graham, M. L., Parker, A., et al. 2010, CBET, 2245, 2
McClelland, C. M., Garnavich, P. M., Milne, P. A., Shappee, B. J., & Pogge, R. W. 2013, ApJ, 767, 119

Meikle, W. P. S., Kotak, R., Farrah, D., et al. 2011, ApJ, 732, 109
Meikle, W. P. S., Mattila, S., Pastorello, A., et al. 2007, ApJ, 665, 608
Milisavljevic, D., Fesen, R., Pickering, T., et al. 2011, CBET, 2946, 2
Milisavljevic, D., Fesen, R. A., Leibundgut, B., & Kirshner, R. P. 2008, ApJ, 684, 1170
Milisavljevic, D., Margutti, R., Kamble, A., et al. 2015, ApJ, 815, 120
Milligan, S., Cranton, B. W., & Skrutskie, M. F. 1996, Proc. SPIE, 2863, 2
Monard, L. A. G., Kneip, R., Brimacombe, J., et al. 2014, CBET, 3977, 1
Monard, L. A. G., Milisavljevic, D., Fesen, R., et al. 2011, CBET, 2946, 1
Morales-Garoffolo, A., et al. 2014, MNRAS, 445, 1647
Mould, J., & Sakai, S. 2008, ApJL, 686, L75
Nakano, S., Sugano, M., Kadota, K., et al. 2013, CBET, 3440, 1
Nakano, S., Yusa, T., Yoshimoto, K., et al. 2012, CBET, 3263, 1
Nozawa, T., Kozasa, T., Umeda, H., Maeda, K., & Nomoto, K. 2003, ApJ, 598, 785
Nozawa, T., Kozasa, T., Tominaga, N., et al. 2008, ApJ, 684, 1343
O'Hara, T. B., Meixner, M., Speck, A. K., Ueta, T., & Bobrowsky, M. 2003, ApJ, 598, 1255
Pilbratt, G. L. 2003, Proc. SPIE, 4850, 586
Pojmanski, G., Prieto, J. L., Stanek, K. Z., & Beacom, J. F. 2008, CBET, 1213, 1
Pugh, H., & Li, W. 2004, IAUC, 8448, 3
Sakon, I., Onaka, T., Wada, T., et al. 2009, ApJ, 692, 546
Salvo, M., Bessell, M., & Schmidt, B. 2003, IAUC, 8187, 1
Salvo, M., Schmidt, B., & Owers, M. 2005, IAUC, 8581, 2
Siviero, A., Tomasella, L., Pastorello, A., et al. 2012, CBET, 3054, 4
Smith, L. J., Crowther, P. A., & Prinja, R. K. 1994, A&A, 281, 833
Smith, N. 2014, ARA&A, 52, 487
Smith, N., Foley, R. J., & Filippenko, A. V. 2008, ApJ, 680, 568
Smith, N., Gehrz, R. D., Campbell, R., et al. 2011, MNRAS, 418, 1959
Smith, N., & Owocki, S. P. 2006, ApJL, 645, L45
Sugerman, B., Meixner, M., Fabbri, J., & Barlow, M. 2004, IAUC, 8442
Sugerman, B. E. K., et al. 2006, Sci, 313, 196
Szalai, T., & Vinkó, J. 2013, A&A, 549, A79
Szalai, T., Vinkó, J., Balog, Z., et al. 2011, A&A, 527, A61
Szalai, T., Vinkó, J., Nagy, A. P., et al. 2016, MNRAS, 460, 1500
Vanbeveren, D., De Loore, C., & Van Rensbergen, W. 1998, A&ARv, 9, 63
Wang, X., Li, W., Filippenko, A. V., et al. 2008, ApJ, 675, 626
Werner, M. W., Roellig, T. L., Low, F. J., et al. 2004, ApJS, 154, 1
Wheeler, J. C., Johnson, V., & Clocchiatti, A. 2015, MNRAS, 450, 1295
Wilson, J. C., Eikenberry, S. S., Henderson, C. P., et al. 2003, Proc. SPIE, 4841, 451
Wooden, D. H., Rank, D. M., Bregman, J. D., et al. 1993, ApJS, 88, 477
Yamaoka, H., Itagaki, K., Guido, E., et al. 2014, CBET, 3795, 2
Zauderer, B. A., Kamble, A., Chakraborti, S., & Soderberg, A. 2014, ATel, 5764, 1